T-matrix approach to quark-gluon plasma

Shuai Y. F. Liu and Ralf Rapp
Cyclotron Institute and Department of Physics and Astronomy, Texas A&M University, College Station, Texas 77843-3366, USA

(Received 16 November 2017; published 29 March 2018)

A self-consistent thermodynamic T-matrix approach is deployed to study the microscopic properties of the quark-gluon plasma (QGP), encompassing both light- and heavy-parton degrees of freedom in a unified framework. The starting point is a relativistic effective Hamiltonian with a universal color force. The input in-medium potential is quantitatively constrained by computing the heavy-quark (HQ) free energy from the static T-matrix and fitting it to pertinent lattice-QCD (lQCD) data. The corresponding T-matrix is then applied to compute the equation of state (EoS) of the QGP in a two-particle irreducible formalism, including the full off-shell properties of the selfconsistent single-parton spectral functions and their two-body interaction. In particular, the skeleton diagram functional is fully resummed to account for emerging bound and scattering states as the critical temperature is approached from above. We find that the solution satisfying three sets of lQCD data (EoS, HQ free energy, and quarkonium correlator ratios) is not unique. As limiting cases we discuss a weakly coupled solution, which features color potentials close to the free energy, relatively sharp quasiparticle spectral functions and weak hadronic resonances near T_c, and a strongly coupled solution with a strong color potential (much larger than the free energy), resulting in broad nonquasiparticle parton spectral functions and strong hadronic resonance states which dominate the EoS when approaching T_c.

DOI: 10.1103/PhysRevC.97.034918

I. INTRODUCTION

Heavy-ion collision experiments at Relativistic Heavy Ion Collider (RHIC) and the Large Hadron Collider (LHC) create the hottest matter ever made by mankind, with temperatures more than 8 orders of magnitude larger than the surface temperature of the sun [1]. It is widely accepted that this matter evolves through a quark-gluon plasma (QGP), a deconfined phase of nuclear matter where the spontaneously broken chiral symmetry is restored. The success of relativistic hydrodynamics in describing light-hadron spectra [2–4], and the surprisingly large modification of heavy-flavor (HF) meson spectra [5] have revealed the hot QCD medium to be a strongly coupled system [6]. However, it currently remains an open issue what the microscopic mechanisms underlying the small viscosity-to-entropy density ratio and HF diffusion coefficient are, and what relevant degrees of freedom of the medium go along with it. It is quite conceivable that the nearby transition from quark-gluon to hadronic matter plays an essential role, and that large collision rates lead to nontrivial spectral functions of the matter constituents. These features are not readily captured by perturbative or quasiparticle approaches; see, e.g., Refs. [7,8] for reviews. On the other hand, the use of lattice-QCD (lQCD) motivated potentials, specifically the heavy-quark (HQ) internal energy, has led to the idea of a bound-state QGP [9,10] as a "transition" medium, with essential contributions from nonperturbative interactions, i.e., remnants of the confining force. For heavy quarks these ideas have been implemented within a thermodynamic T-matrix approach [11–15], thereby connecting the open and hidden HF sectors. This framework has met fair success in understanding pertinent low-momentum HF observables in ultrarelativistic heavy-ion collisions (URHICs), and has reinforced the need for a more rigorous determination of the underlying two-body interaction, rather than bracketing it by the free and internal energies which roughly correspond to a weakly and strongly coupled scenario, respectively. In a lQCD-based extraction [16], it was found that the static potential is close to the free energy while the associated imaginary part is near expectations from hard-thermal-loop perturbation theory. In Ref. [17] the HQ free energy was calculated within the T-matrix formalism where the underlying potential was defined as the driving kernel in the corresponding integral equation. It was found that, in the presence of large imaginary parts of the static quarks, the lQCD data support a solution where the potential rises well above the free energy. Furthermore, implementing this potential in a self-consistent quantum many-body framework [the Luttinger-Ward-Baym (LWB) formalism] [18–20], a description of the equation of state (EoS) of the QGP was achieved where parton spectral functions become very broad, losing their quasiparticle nature at low momenta, and the degrees of freedom change to broad hadronic states as the transition temperature is approached from above [21].

In the present paper, we expand on our previous studies by setting up a unified LWF formalism to investigate the microscopic properties of light, heavy, and static degrees of freedom of the QGP, and firmly root it in information available from thermal lQCD. Our starting point is an effective Hamiltonian in quark and gluon degrees of freedom with a color interaction of Cornell potential-type, including relativistic corrections. While this approach reduces to potential nonrelativistic QCD in the HQ limit we here pursue the question in how far the interactions encoded in the potential approximation (including remnants of the confining force) are relevant for understanding bulk and spectral properties of the QGP. We also note that

the vacuum potential model using the Cornell interaction has met with fair success in light-hadron spectroscopy (with caveats for spontaneous chiral symmetry breaking and its Goldstone bosons) [22–24]. We determine the input to our Hamiltonian by systematically constraining the interaction through the static HQ free energies, Euclidean correlators for charmonia and bottomonia, and the EoS in the light sector with two additional effective-mass parameters for light quarks and gluons. As mentioned above, a key feature of this approach is to retain the full off-shell properties of one- and two-body spectral functions (and scattering amplitudes), which renders the emerging microstructure of the QGP a prediction of the formalism. Since the latter is directly formulated in real time, transport coefficients (η/s or the HF diffusion coefficients, $\mathcal{D}_s$) [25] and other quantities of experimental interest (e.g., photon and dilepton production rates) can be readily computed. As it will turn out, the self-consistent solution to the 3 sets of lQCD data is not unique. We will therefore discuss limiting cases of the underlying force strength, elaborate on the pertinent consequences for QGP structure and indicate ways to further constrain the "correct" scenario.

This paper is organized as follows. In Sec. II we introduce the effective Hamiltonian and the three-dimensional (3D) relativistic T-matrix approach used in this work. In Sec. III we lay out how the latter can be systematically constrained via various quantities computed in lQCD, namely: the EoS of the QGP using the LWB formalism (Sec. III A), including a matrix-log technique to resum the skeleton diagram (two-body interaction) contribution, the static HQ free energies (Sec. III B), and quarkonium correlators (Sec. III C), including interference effects in the imaginary part of the potential; in Sec. III D we introduce our ansatz for the in-medium potential (Sec. III D 1) and describe the concrete procedure for carrying out the overall self-consistent fit (Sec. III D 2). In Sec. IV we show and discuss the main numerical results in comparison to lQCD data, specifically for what we will denote as a "weakly coupled solution" (WCS, Sec. IV A) and a "strongly coupled solution" (SCS, Sec. IV B); each of these solutions is elaborated in four parts, pertaining to the potential extraction via fits to the HQ free energy (Secs. IV A 1 and IV B 1), Euclidean quarkonium correlator ratios, and associated quarkonium spectral functions (Secs. IV A 2 and IV B 2), the fits to the EoS and its (change in) underlying degrees of freedom (Secs. IV A 3 and IV B 3), and the resulting parton spectral functions in heavy and light sectors with corresponding two-body T-matrices (Secs. IV A 4 and IV B 4). In Sec. V we summarize our findings and outline future directions and opportunities within our approach. In the Appendix we collect further information on more general aspects of the relativistic potential approach (Appendix A), generalized thermodynamic relations within the LWB formalism for an effective in-medium Hamiltonian (Appendix B), additional relations involving the static-potential limit (Appendix C), and a discussion of interference effects in its imaginary part (Appendix D).

II. THERMODYNAMIC T-MATRIX

Bound states are key entities of the nonperturbative physics of a quantum system, especially in QCD where the hadrons encode the phenomena of confinement and mass generation. In diagram language, bound states require an infinite resummation of (ladder) diagrams, represented by an integral equation such as the 4D Bethe-Salpeter (BS) equation [26] or a 3D reduced T-matrix equation [27–29]. Both equations allow for a simultaneous and straightforward treatment of scattering states. As a resummed series, the solution of the integral equation analytically continues to the strongly coupled region.[1] This equation is therefore well suited to study the strongly coupled QGP (sQGP) near T_c where both bound and scattering states are expected to be important and entangled with each other in the presence of strong quantum effects, i.e., large scattering rates. Applications of the T-matrix approach in media has been carried out in various contexts, mostly in nonrelativistic many-body systems [32–34] but also in systems where relativistic effects are relevant [35], e.g., the nuclear many-body problem [36,37], hot hadronic matter [38], or the QGP [10,21,25,39,40].

In the present work our starting point is a Hamiltonian with relativistic dispersion relations and potential, which maps onto the Thompson scheme [28] for the 3D reduction from the BS to the T-matrix equation (as employed earlier in the HQ sector [13]). It can be written in the form

$$H = \sum \varepsilon_i(\mathbf{p})\psi_i^\dagger(\mathbf{p})\psi_i(\mathbf{p}) + \frac{1}{2}\psi_i^\dagger\left(\frac{\mathbf{P}}{2}-\mathbf{p}\right) \times \psi_j^\dagger\left(\frac{\mathbf{P}}{2}+\mathbf{p}\right)V_{ij}^a\psi_j\left(\frac{\mathbf{P}}{2}+\mathbf{p}'\right)\psi_i\left(\frac{\mathbf{P}}{2}-\mathbf{p}'\right), \quad (1)$$

where $\varepsilon_i(\mathbf{p}) = \sqrt{M_i^2+\mathbf{p}^2}$ and $\mathbf{P}$ is the total momentum of the two-particle state. The summations over i,j include momentum, spin, color, and particle species (three light-quark flavors and gluons for the bulk matter description, or charm and bottom flavors for pertinent correlation functions). The index "a" specifies the two-body color channels. In this paper, we do not account for spin-dependent interaction, which are expected to be subleading but can be included in the future. For the potential, V, we include both color-Coulomb ($V_\mathcal{C}$) and (remnants of the) confining ("string") interaction ($V_\mathcal{S}$),

$$V_{ij}^a(\mathbf{p},\mathbf{p}') = \mathcal{R}_{ij}^\mathcal{C}\mathcal{F}_a^\mathcal{C}V_\mathcal{C}(\mathbf{p}-\mathbf{p}') + \mathcal{R}_{ij}^\mathcal{S}\mathcal{F}_a^\mathcal{S}V_\mathcal{S}(\mathbf{p}-\mathbf{p}'). \quad (2)$$

Relativistic effects in the vertices of the 4D theory are included by introducing relativistic factors $\mathcal{R}$ [13,41],

$$\mathcal{R}_{ij}^\mathcal{C} = \sqrt{1+\frac{p^2}{\varepsilon_i(p)\varepsilon_j(p)}}\sqrt{1+\frac{p'^2}{\varepsilon_i(p')\varepsilon_j(p')}}, \quad (3)$$

$$\mathcal{R}_{ij}^\mathcal{S} = \sqrt{\frac{M_iM_j}{\varepsilon_i(p)\varepsilon_j(p)}}\sqrt{\frac{M_iM_j}{\varepsilon_i(p')\varepsilon_j(p')}}, \quad (4)$$

and $\mathcal{F}^{\mathcal{C},\mathcal{S}}$ are color factors in diagonal representation; specifically, the Coulomb factors, $\mathcal{F}^\mathcal{C}$, are the standard Casimir coefficients [9,13] collected in Table I, while for the string factors, $\mathcal{F}^\mathcal{S}$, we take the absolute values of the Casimir

[1] The series $1+\alpha+\alpha^2\cdots = 1/(1-\alpha)$ is convergent for strong coupling. Divergence at strong coupling is different from the $N!$ divergence of a perturbative series at small coupling [30,31].

TABLE I. Casimir and degeneracy factors for different color channels quoted as (Casimir factor, degeneracy).

qq	$q\bar{q}$	$(q/\bar{q})g$	gg
(1/2, 3)	(1, 1)	(9/8, 3)	(9/4, 1)
(−1/4, 6)	(−1/8, 8)	(3/8, 6)	(9/8, 16)
		(−3/8, 15)	(−3/4, 27)

coefficients, to ensure a positive definite string tension, which appears to be weaker in colored channels [42]. The precise form of V_C, V_S, and the parton mass values, M_i, are inputs to the Hamiltonian that need to be constrained by the lQCD data to be discussed in the following sections.

The finite-temperature calculations are carried out in the Matsubara formalism, where the "bare" propagators for both quarks and gluons are taken as

$$G_i^0(i\omega_n,\mathbf{p}) = \frac{1}{i\omega_n - \varepsilon_i(\mathbf{p})}. \quad (5)$$

We resum the ladder diagrams of the Hamiltonian by the T-matrix equation, pictorially displayed in Fig. 1. In the center-of-mass (CM) frame it can be written as

$$T_{ij}^a(z,\mathbf{p},\mathbf{p}') = V_{ij}^a(\mathbf{p},\mathbf{p}') + \int_{-\infty}^{\infty} \frac{d^3\mathbf{k}}{(2\pi)^3} V_{ij}^a(\mathbf{p},\mathbf{k}) G_{ij}^0(z,\mathbf{k}) T_{ij}^a(z,\mathbf{k},\mathbf{p}'), \quad (6)$$

where $z = iE_n$ is the two-body Matsubara frequency (or analytical energy variable $E \pm i\epsilon$), and $\mathbf{p},\mathbf{p}'$ are the incoming and outgoing 3-momenta, respectively, for each parton in the CM frame, i.e., for total momentum $\mathbf{P} = 0$; $T_{ij}^a(z,\mathbf{p},\mathbf{p}')$ denotes the T-matrix between particle type i and j in color channel a. The two-body propagator is defined in Matsubara representation as

$$G_{ij}^0(iE_n,\mathbf{k}) = -\beta^{-1} \sum_{\omega_n} G_i(iE_n - i\omega_n,\mathbf{k}) G_j(i\omega_n,\mathbf{k}), \quad (7)$$

and, using a spectral representation, can be written in terms of single-particle spectral functions as

$$G_{ij}^0(z,\mathbf{k}) = \int_{-\infty}^{\infty} d\omega_1 d\omega_2 \frac{[1 \pm n_i(\omega_1) \pm n_j(\omega_2)]}{z - \omega_1 - \omega_2} \times \rho_i(\omega_1,\mathbf{k}) \rho_j(\omega_2,\mathbf{k}), \quad (8)$$

with the single-particle propagators

$$G_i(z) = \frac{1}{\left[G_i^0(z,k)\right]^{-1} - \Sigma_i(z,k)} = \frac{1}{z - \varepsilon_i(p) - \Sigma_i(z,k)},$$

$$\rho_i(\omega,\mathbf{k}) = -\frac{1}{\pi} \mathrm{Im} G_i(\omega + i\epsilon). \quad (9)$$

In Eq. (8) the $\pm$ sign refers to bosons (upper) and fermions (lower), and n_i is the Bose or Fermi distribution function

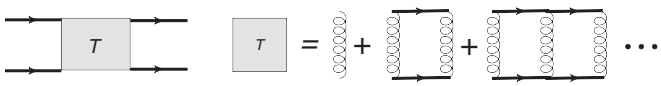

FIG. 1. T-matrix resummation for ladder diagrams.

for parton i. The in-medium self-energies, $\Sigma_i(z,k)$, will be self-consistently computed through the two-body T-matrix, as detailed below.

In vacuum it is sufficient to solve the T-matrix in the CM frame due to Lorentz invariance. However, in medium, Lorentz invariance is in general broken, although usually not by much for the scattering amplitude at total momenta comparable to the thermal scale in nondegenerate media. Thus, a standard approximation is to assume the in-medium T-matrix to be independent of $\mathbf{P}$ [13,14], which leads to a major simplification of the calculations. We thus write

$$T_{ij}^a(\omega_1+\omega_2,\mathbf{p}_1,\mathbf{p}_2|\mathbf{p}_1',\mathbf{p}_2') = T_{ij}^a(E_{\rm cm},p_{\rm cm},p_{\rm cm}',x_{\rm cm}), \quad (10)$$

where $E_{\rm cm}$, $p_{\rm cm}$, $p_{\rm cm}'$, and $x_{\rm cm} \equiv \cos(\theta_{\rm cm})$ are functions expressed via $\omega_1+\omega_2,\mathbf{p}_1,\mathbf{p}_2,\mathbf{p}_1',\mathbf{p}_2'$ using momentum conservation $\mathbf{p}_1+\mathbf{p}_2 = \mathbf{p}_1'+\mathbf{p}_2'$ to define the transformation to the CM frame:

$$E_{\rm cm} = \sqrt{(\omega_1+\omega_2)^2 - (\mathbf{p}_1+\mathbf{p}_2)^2},$$
$$s_{\rm on} = (\varepsilon_1(\mathbf{p}_1)+\varepsilon_2(\mathbf{p}_2))^2 - (\mathbf{p}_1+\mathbf{p}_2)^2,$$
$$p_{\rm cm} = \sqrt{\frac{\left(s_{\rm on} - M_i^2 - M_j^2\right)^2 - 4M_i^2M_j^2}{4s_{\rm on}}},$$
$$\cos(\theta_{\rm cm}) = \frac{\mathbf{p}_{\rm cm}\cdot\mathbf{p}_{\rm cm}'}{p_{\rm cm}p_{\rm cm}'}. \quad (11)$$

For $p_{\rm cm}'$, we simply change $s_{\rm on}(\mathbf{p}_1,\mathbf{p}_2)$ to $s_{\rm on}(\mathbf{p}_1',\mathbf{p}_2')$. The reason for using the on-shell s for $p_{\rm cm}$ is to keep the analytical properties of the T-matrix after the transformation. Also, this transformation recovers Galilean invariance in the nonrelativistic limit for the off-shell case. The relation for $p_{\rm cm}$ can be derived by solving the equations originating from Lorentz invariants $\varepsilon_1(\mathbf{p}_1)^2 - p_1^2 = M_1^2$, $\varepsilon_2(\mathbf{p}_2)^2 - p_2^2 = M_1^2$ and $\varepsilon_1[(\mathbf{p}_1)+\varepsilon_2(\mathbf{p}_2)]^2 - (\mathbf{p}_1+\mathbf{p}_2)^2 = [\varepsilon_1(\mathbf{p}_{\rm cm})+\varepsilon_2(\mathbf{p}_{\rm cm})]^2$ in the CM and the moving frame. We note that this procedure does not work for the CM angle in the off-shell case. However, since we only need forward scattering amplitudes for our present purposes, we do not discuss this issue any further here.

Rotational symmetry in the CM frame implies that a partial-wave expansion remains intact, given by

$$X(\mathbf{p},\mathbf{p}') = 4\pi \sum_l (2l+1) X^l(p,p') P_l[\cos(\theta)], \quad (12)$$

where $X = V,T$. The partial-wave expanded scattering equation becomes

$$T_{ij}^{l,a}(z,p,p') = V_{ij}^{l,a}(p,p') + \frac{2}{\pi}\int_{-\infty}^{\infty} k^2 dk V_{ij}^{l,a}(p,k) G_{ij}^0(z,k) \times T_{ij}^{l,a}(z,k,p'), \quad (13)$$

where l denotes the angular-momentum quantum number. The set of now 1D integral equations can be solved by discretizing the 3-momenta p,p',k,

$$\mathbb{V}_{mn} \equiv V(k_m,k_n), \quad \hat{\mathbb{G}}_{(2)}^0(z)_{mn} \equiv \frac{2\Delta k}{\pi} k_m^2 G_{(2)}^0(z,k_m)\delta_{mn} \quad (14)$$

and invert the pertinent matrix equation [43],

$$\mathbb{T}(z)_{mn} = T(z,k_m,k_n), \mathbb{T}(z) = \left[\mathbb{1} - \mathbb{V}\hat{\mathbb{G}}_{(2)}^0(z)\right]^{-1}\mathbb{V}. \quad (15)$$

The integral over k in Eq. (13) is encoded in a matrix multiplication with measure dk. Here and in the following, we (occasionally) use the subscript "(2)" as an abbreviation for "ij" to denote two-body quantities.

Once the T-matrices have been computed, we calculate the single-particle self-energies by summing over all partial waves and the pertinent two-body flavor and color channels in interactions with light medium partons. Closing the T-matrix with an in-medium single-parton propagator ($\pm$ for boson/fermion) in the Matsubara formalism,

$$\Sigma(i w_n) = \pm \frac{-1}{\beta} \sum_{\nu_n} T(i\omega_n + i\nu_n) G(i\nu_n), \tag{16}$$

one can use spectral representations to carry out the summation over discrete frequencies to obtain

$$\Sigma_i(z,\mathbf{p}_1) = \int \frac{d^3\mathbf{p}_2}{(2\pi)^3} \int_{-\infty}^{\infty} d\omega_2 \frac{dE}{\pi} \frac{-1}{z+\omega_2-E} \frac{1}{d_i} \sum_{a,j} d_s^{ij} d_a^{ij} \times \mathrm{Im}T_{ij}^a(E,\mathbf{p}_1,\mathbf{p}_2|\mathbf{p}_1,\mathbf{p}_2)\rho_j(\omega_2,\mathbf{p}_2) \times [n_j(\omega_2) \mp n_{ij}(E)], \tag{17}$$

which involves the forward-scattering amplitude, i.e., $\mathbf{p}_1' = \mathbf{p}_1$ and $\mathbf{p}_2' = \mathbf{p}_2$ and thus $x_{\rm cm} = x = 1$; n_{ij} refers to the Bose or Fermi distribution appropriate for the two-body state ij, but the "$-/+$" sign refers to the bosonic/fermionic single-parton state i. The $d_{a,s}^{ij}$ are color and spin degeneracy factors of the two-body system, summarized in Table I. Here, we enforce two physical polarizations for the gluons; d_i is the spin-color degeneracy of the single parton i. The energy, $z = \omega_1 + i\varepsilon$, is taken to be retarded in this work. Within the CM transformation defined via Eqs. (11), the integrations in Eq. (17) are restricted to the timelike two-body phase, i.e., real values for $E_{\rm cm}$ [we have verified that $\mathrm{Im}T_{ij}^a(\sqrt{E^2-P^2})$ is strongly suppressed when approaching the spacelike region]. The above self-energy expression does not include the purely real thermal Fock term [44], which we add explicitly by calculating

$$\Sigma_i(\mathbf{p}_1) = \mp \int \frac{d^3\mathbf{p}_2}{(2\pi)^3} \int_{-\infty}^{\infty} d\omega_2 V_{ii}^1(\mathbf{p}_1-\mathbf{p}_2)\rho_i(\omega_2,\mathbf{p}_2) n_i(\omega_2). \tag{18}$$

Finally, we recall that Eq. (17) can be expressed a functional equation of Σ,

$$\Sigma = T(\Sigma)G(\Sigma) = T(\Sigma)\frac{1}{(G^0)^{-1}-\Sigma}. \tag{19}$$

It is equivalent to an integral equation for the full Green function, G, as $\Sigma = (G^0)^{-1} - G^{-1}$. The T-matrix depends on the self-energy, $T(\Sigma)$, through the two-body propagator, see Eq. (8), in which the spectral function depends on the single-parton self-energy; see Eq. (9). Although it is a nonlinear functional equation, it usually can be solved self-consistently. The self-energy as the solution of Eq. (19) satisfies conservation laws for the Green function [19].

III. CONSTRAINTS FROM LATTICE QCD

The Hamiltonian given in Eq. (1) is the input to our approach that needs to be constrained by independent information. To achieve this, we will make extensive use of first-principles lQCD computations, where we treat the pertinent data as "observables" in imaginary time. Specifically, we will utilize the QGP EoS [45,46], HQ free energies [42,47,48], and Euclidean quarkonium correlators [49–52]. In this section, we elaborate on the concrete procedure to do that, which includes theoretical developments to best take advantage of the comparisons within the T-matrix approach. In Sec. III A we briefly recapitulate the LWB formalism [18–20] to compute the in-medium single- and two-body interaction contributions to the EoS for the effective Hamiltonian and lay out the corresponding matrix-log technique to resum the pertinent skeleton diagrams [21,25]. In Sec. III B we recall the formalism to calculate the static-quark free energy from the T-matrix, where large imaginary parts turn out to play a critical role [17]. In Sec. III C we briefly review the formalism to calculate quarkonium correlator ratios based on Refs. [11,13,14], thereby introducing an effective way to account for interference effects in the complex potential for quarkonium spectral functions.

A. Equation of state

The equation of state (EoS) usually refers to the pressure as a function energy density, or, alternatively, as a function of temperature and chemical potential of a many-body system, $P(T,\mu)$. It characterizes the macroscopic dynamics of the bulk which are ultimately driven by the relevant microscopic degrees of freedom of the medium. Although the EoS depends on the interactions in the system, it is usually most sensitive to the masses of the prevalent degrees of freedom in the medium (which, however, may be generated dynamically through the interactions, e.g., via bound-state formation). Therefore, comparing the calculated EoS with lQCD results is expected to primarily constrain the "bare" parton masses in the Hamiltonian, Eq. (1).

For a homogeneous grand canonical ensemble, the EoS is encoded in the grand potential (per unit volume), $\Omega = -P$, which can be calculated using diagrammatic techniques within the LWB formalism [18–20] (for recent application to QCD matter, see also Refs. [7,53,54]) as spelled out in Sec. III A 1. Since the QGP near T_c can be expected to be a mixture of interacting partons and their bound states, a nonperturbative ladder resummation for the two-body amplitudes is in order. Some care needs to be exerted since the ladder resummation to calculate Ω is not the same as for the T-matrix, due to a double-counting when closing the external legs of the latter. This will be carried out using a matrix-logarithm resummation technique [21,25] detailed in Sec. III A 2.

1. Properties of the LWB formalism

The diagram language of the LWB formalism leads to the following expression for grand potential:

$$\Omega = \mp \frac{-1}{\beta} \sum_n \mathrm{Tr}\{\ln(-G^{-1}) + [(G^0)^{-1} - G^{-1}]G\} \pm \Phi, \tag{20}$$

where we combined spin, color, flavor, and momentum summations in the trace operation, "Tr", while explicitly writing

the Matsubara frequency sum, $\sum_n$. Here,

$$\Phi = \sum_{\nu=1}^{\infty} \Phi_\nu \tag{21}$$

denotes the Luttinger-Ward functional (LWF), and

$$\Phi_\nu = \frac{-1}{\beta} \sum_n \mathrm{Tr}\left\{ \frac{1}{2\nu} \left(\frac{-1}{\beta} \right)^\nu [(-\beta)^\nu \Sigma_\nu(G)] G \right\} \tag{22}$$

and $\Sigma_\nu(G)$ are the LWF and self-energy at νth order of the potential in the "skeleton" expansion [18]. These three quantities should be understood as functionals of the full single-particle propagator, G. The full self-energy is the sum of all self-energies of order ν, $\Sigma(G) = \sum_\nu \Sigma_\nu(G)$. The extra factor $1/\nu$ in Eq. (22) complicates the resummation of $\Phi(\Sigma_\nu)$ for ladder diagrams, to be discussed in the next section. The factor $(-1/\beta)^\nu(-\beta)^\nu$ aims to separate out the $-1/\beta$ temperature dependence from loop integrals in the self-energy, such as $-1/\beta \sum_n X_1(\omega_n) X_2(z_m - \omega_n)$. At νth order, there are ν loops, with the pertinent factor $(-1/\beta)^\nu$. After this separation, $[(-\beta)^\nu \Sigma_\nu(G)]$ only has a temperature dependence stemming from G and the interaction kernel, V. This separation procedure is convenient for proving thermodynamic relations involving temperature derivatives, cf. Appendix B.

The skeleton diagram expansion for the self-energy can be obtained via a functional derivative of Φ,

$$\Sigma(G) = \frac{\delta \Phi}{\delta G}. \tag{23}$$

The functional derivative is equivalent to cut open one G line in a closed loop [18]. Since there are ν equivalent G lines at νth order, this cancels the factor $1/\nu$ and recovers the full self-energy. With the help of Eq. (23) one finds the thermodynamic potential to reach an extremum,

$$\frac{\delta \Omega}{\delta G} = 0, \tag{24}$$

when the functional relation

$$\Sigma(G) = (G^0)^{-1} - G^{-1} \tag{25}$$

is satisfied. In this sense, G acts like a functional order parameter for the thermodynamic potential to reach an extremum.

In a slight variation of the standard LWB formalism, the "bare" masses [or dispersion relations, $\varepsilon(\mathbf{p})$] and potential of our effective Hamiltonian depend on temperature T and chemical potential μ_q of the medium. These dependencies represent a macroscopic average over the microphysics that we do not treat explicitly (such as remaining gluonic condensates in the QGP that can induce mass terms and the nonperturbative string term in the potential). This leads to modified expressions for several thermodynamic relations, e.g., more complicated relations for energy and entropy to reconstruct the pressure; this is elaborated in Appendix B.

2. *Matrix logarithm resummation of skeleton diagrams*

The main challenge in calculating the grand potential, Ω, is to evaluate the LWF, Φ. In our derivation we limit ourselves to the case of a 3D reduced T-matrix, rather than the more general 4D BS equation discussed in Ref. [25], expanding on what we indicated earlier in Ref. [21].

Using the notation $\int d\tilde{p} \equiv -\beta^{-1} \sum_n \int d^3\mathbf{p}/(2\pi)^3$ with $\tilde{p} \equiv (i\omega_n, \mathbf{p})$, the νth order of the self-energy appearing in Eq. (20) in ladder approximation can be formally written as

$$\Sigma_\nu(G) = \int d\tilde{p} \left[V G^0_{(2)} V G^0_{(2)} \cdots V \right] G, \tag{26}$$

containing ν factors of V. Thus, the LWF functional Φ can be expressed as

$$\Phi = \frac{1}{2} \sum \mathrm{Tr}\left\{ G \left[V + \frac{1}{2} V G^0_{(2)} V + \ldots + \frac{1}{\nu} V G^0_{(2)} V G^0_{(2)} \ldots . V + \ldots \right] G \right\}, \tag{27}$$

where "Tr" denotes, as before, a 3-momentum integral and the summation over discrete quantum numbers, while $\sum$ denotes the sum over Matsubara frequencies including β factors. The part in brackets, $[\cdots]$, has a structure very similar to the T-matrix resummation,

$$\begin{aligned} T &= V + V G^0_{(2)} V + \ldots + V G^0_{(2)} V G^0_{(2)} \ldots V + \ldots \\ &= \left[\sum_{\nu=0}^{\infty} \left(V G^0_{(2)} \right)^\nu \right] V = [1 - V G^0_{(2)}]^{-1} V, \end{aligned} \tag{28}$$

except for the extra coefficients $1/\nu$. However, we can write

$$\begin{aligned} & V + \frac{1}{2} V G^0_{(2)} V + \cdots + \frac{1}{\nu} V G^0_{(2)} V G^0_{(2)} \ldots V + \cdots \\ &= \left[\sum_{\nu=1}^{\infty} \frac{1}{\nu} \left(V G^0_{(2)} \right)^\nu \right] \left[G^0_{(2)} \right]^{-1} \\ &= -\ln \left[1 - V G^0_{(2)} \right] \left[G^0_{(2)} \right]^{-1} \equiv \mathrm{Log}\, T, \end{aligned} \tag{29}$$

where the (natural-base) logarithm is to be understood as a general matrix operation (in a discrete space of quantum numbers, including spin, color, flavor as well as energy-momentum), defined through its power series.[2] It can also be tested in the case of a separable potential for which the analytical result is known [57]. At large coupling, the perturbative series does not converge (in the present context, we have checked this, e.g., for the HQ friction coefficient discussed in Ref. [25]) and does not capture the formation of bound states which are expected to become important at low temperatures, cf. also footnote 1.

The similarity between the T-matrix and the Log T operation further allows us to migrate the partial-wave expansion, Eq. (13), and CM approximation, Eq. (6), from the T-matrix to the LWF. With the numerical discretization of the 3-momentum integrals as in Eqs. (14) and (15), we can define Log $T^{l,a}_{ij}$ in a given channel as

$$\begin{aligned} \mathbb{L}\mathrm{og}\mathbb{T}(z)_{mn} &\equiv \mathrm{Log}\, T(z, k_m, k_n), \\ \mathbb{L}\mathrm{og}\mathbb{T}(z) &= -\mathbb{L}\mathrm{og}\left[\mathbb{1} - \mathbb{V}\hat{\mathbb{G}}^0_{(2)}(z) \right] \left[\hat{\mathbb{G}}^0_{(2)}(z) \right]^{-1}. \end{aligned} \tag{30}$$

[2] A similar expression is known for the ground-state energy at zero temperature [55] and for cold-atom systems [56].

Compared to the T-matrix Eq. (15), the only change is replacing the inverse matrix (with an extra factor $\mathbb{V}$) by the "matrix-Log" operation, $\mathbb{L}\mathrm{og}\mathbb{T}$ (with an extra factor $[\hat{\mathbb{G}}^0_{(2)}(z)]^{-1}$). Standard software like Mathematica can compute this matrix function at a speed similar to a matrix inversion. With the result in a given channel, we first sum over partial waves using Eq. (12) and then transform back from the CM to an arbitrary frame using Eq. (10) with $E_{\rm cm}$, $p_{\rm cm}$, $p'_{\rm cm}$, and $x'_{\rm cm}$ defined in Eq. (11),

$$\mathrm{Log}T^a_{ij}(\omega_1+\omega_2,\mathbf{p}_1,\mathbf{p}_2|\mathbf{p}'_1,\mathbf{p}'_2)=\mathrm{Log}T^a_{ij}(E_{\rm cm},p_{\rm cm},p'_{\rm cm},x_{\rm cm}). \tag{31}$$

Upon closing two external lines of this quantity with a thermal single-particle propagator, G, and, in resemblance of Eq. (17), defining

$$\mathrm{Log}\,\Sigma\equiv\int d\tilde{p}\,\mathrm{Log}\,TG, \tag{32}$$

we obtain

$$\begin{aligned}\mathrm{Log}\Sigma_i(z,\mathbf{p}_1)=&\int\frac{d^3\mathbf{p}_2}{(2\pi)^3}\int_{-\infty}^{\infty}d\omega_2\frac{dE}{\pi}\frac{-1}{z+\omega_2-E}\\&\times\frac{1}{d_i}\sum_{a,j}d_s^{ij}d_a^{ij}\mathrm{Im}\big[\mathrm{Log}T^a_{ij}(E,\mathbf{p}_1,\mathbf{p}_2|\mathbf{p}_1,\mathbf{p}_2)\big]\\&\times\rho_j(\omega_2,\mathbf{p}_2)[n_j(\omega_2)\mp n_{ij}(E)].\end{aligned} \tag{33}$$

Recalling Eq. (27) and the definition of $\mathrm{Log}\Sigma$ and $\mathrm{Log}T$, we can express the LWF as

$$\begin{aligned}\Phi&=\frac{1}{2}\int d\tilde{p}G\mathrm{Log}\Sigma\\&=\frac{1}{2}\sum_j d_j\int d\tilde{p}G_j(\tilde{p})\mathrm{Log}\Sigma_j(\tilde{p}).\end{aligned} \tag{34}$$

Therefore, the grand potential in Eq. (20) can be expressed in closed form as

$$\begin{aligned}\Omega=\sum_j\mp d_j\int d\tilde{p}\Big\{&\ln(-G_j(\tilde{p})^{-1})\\&+\Big[\Sigma_j(\tilde{p})-\frac{1}{2}\mathrm{Log}\Sigma_j(\tilde{p})\Big]G_j(\tilde{p})\Big\}.\end{aligned} \tag{35}$$

The final sum over Matsubara frequencies in Eq. (35) can be carried out with usual contour techniques utilizing a spectral representation of the expression in "{ }" as a whole. Through this resummation we include the contributions of the diagrams shown in Fig. 2 to the grand potential Ω.

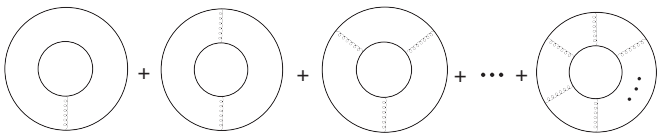

FIG. 2. Examples of diagrams that are resummed by the generalized T-matrix for EoS.

B. Static $Q\bar{Q}$ free energy

The HQ free energy, $F_{Q\bar{Q}}(r,T)$, is commonly defined as the change in free energy of a system when adding to it a static quark and antiquark, separated by a distance r [not including the (infinite) HQ masses]. In the vacuum, this simply corresponds to the potential energy between them. In medium, the free energy and the potential are still related to each other, but no longer identical [9,17,58], as the former includes the response of the medium to the static charges, encoded in the generally complex HQ self-energies. However, one can *calculate* the free energy from an underlying potential within the same T-matrix approach that we discussed for the EoS above, by taking the limit $M_Q\to\infty$ [17]. This opens the possibility to extract (or at least constrain) the driving kernel of the Hamiltonian through a fit to high-precision lQCD data for $F_{Q\bar{Q}}(r,T)$. In particular, since the free energy incorporates the response of the medium to the external source, we need to couple the static quarks with the light partons of the QGP medium consistently. This is achieved by the HQ self-energy in the QGP which we compute from the in-medium heavy-light T-matrix with the same underlying driving kernel. In the following, we first recall some basic relations for the free energy, in particular, how it is related to the driving kernel of the static T-matrix (Sec. III B 1). Second, we discuss the self-consistent extraction of the potential which makes contact with the QGP bulk medium (Sec. III B 2). In Appendix C we collect several additional relations implied by the formalism, and in Appendix D we elaborate on the connection between interference effects and the "imaginary part of potential."

1. Heavy-quark free energy and potential

In this section, we recall the derivation to relate $F_{Q\bar{Q}}(r,T)$ with the color-singlet potential in the static limit, $V(r,T)$ [17] where we suppress color-flavor indices for simplicity in this section.

The static limit introduces simplifications which renders the relation between free energy and the potential rather straightforward. The source of this simplification is the one-particle propagator in the infinite-mass limit [59],

$$\begin{aligned}G_Q(z,\mathbf{r}')&=\int\frac{d^3\mathbf{p}'}{(2\pi)^3}e^{i\mathbf{p}'\cdot\mathbf{r}'}\frac{1}{z-\varepsilon_{\mathbf{p}'}-\Sigma_Q(z,\mathbf{p}')}\\&\approx\int\frac{d^3\mathbf{p}'}{(2\pi)^3}e^{i\mathbf{p}'\cdot\mathbf{r}'}\frac{1}{z-M-\Sigma_Q(z)}=\delta(\mathbf{r}')G_Q(z).\end{aligned} \tag{36}$$

The δ function signifies that the particle is static and $G_Q(z)=1/[z-M-\Sigma_Q(z)]$ is simply the propagator in momentum space in the static limit, i.e., it is localized at its position. At vanishing quark chemical potential, $G_Q=G_{\bar{Q}}$. The two-body (four-point) Green's function inherits the δ-function structure [59],

$$\begin{aligned}&G^>_{Q\bar{Q}}(-i\tau,\mathbf{r}_1,\mathbf{r}_2|\mathbf{r}'_1,\mathbf{r}'_2)\\&\quad\equiv\delta(\mathbf{r}_1-\mathbf{r}'_1)\delta(\mathbf{r}_2-\mathbf{r}'_2)G^>_{Q\bar{Q}}(-i\tau,r),\end{aligned} \tag{37}$$

where $r=|\mathbf{r}_1-\mathbf{r}_2|$. Here, $G^>_{Q\bar{Q}}(-i\tau,r)$ denotes the reduced Green function with the spatial δ functions factored out. The

static $Q\bar{Q}$ free energy, $F_{Q\bar{Q}}$, can be defined in terms of the $Q\bar{Q}$ Green function as [59]

$$F_{Q\bar{Q}}(r,\beta) = -\frac{1}{\beta}\ln[G^{>}_{Q\bar{Q}}(-i\beta,r)]. \tag{38}$$

The remaining task is to calculate the Euclidean time Green function, $G^{>}_{Q\bar{Q}}(-i\tau,r)$, in Eq. (37) using the T-matrix, Eq. (6), with the propagators $G_Q(z)$ and potential $V(z,\mathbf{p}_1-\mathbf{p}'_1)$, which in coordinate space is denoted as $V(z,r)$. We here keep a dependence of the potential on the total energy, z, of the 2-particle system, which can arise, e.g., from interference effects as illustrated in Appendix C.

To proceed, we first use $G_{Q,\bar{Q}}(z)$ to obtain the noninteracting two-body propagator figuring in the T-matrix,

$$G^0_{Q\bar{Q}}(z) = \int_{-\infty}^{\infty} d\omega_1 d\omega_2 \frac{\rho_Q(\omega_1)\rho_{\bar{Q}}(\omega_2)}{z-\omega_1-\omega_2}, \tag{39}$$

where $\rho_{Q/\bar{Q}}(\omega_1)$ are the spectral functions of the static quark/antiquark, as before. Inserting this propagator together with $V(z,\mathbf{p}_1-\mathbf{p}'_1)$ into Eq. (6), one has

$$\begin{aligned} T_{Q\bar{Q}}(z,\mathbf{p},\mathbf{p}') &= V(z,\mathbf{p}-\mathbf{p}') \\ &\quad + \int \frac{d^3\mathbf{k}}{(2\pi)^3} V(z,\mathbf{p}-\mathbf{k}) G^0_{Q\bar{Q}}(z) T_{Q\bar{Q}}(z,\mathbf{k},\mathbf{p}'). \end{aligned} \tag{40}$$

Since $G^0_{Q\bar{Q}}(z)$ is independent of momentum, Fourier transforming the above equation from $\mathbf{p}\to\mathbf{r}$ and $\mathbf{p}'\to\mathbf{r}'$, where $\mathbf{r}=\mathbf{r}_1-\mathbf{r}_2$ and $\mathbf{r}'=\mathbf{r}'_1-\mathbf{r}'_2$, one arrives at

$$\begin{aligned} T_{Q\bar{Q}}(z,\mathbf{r},\mathbf{r}') &= V(z,r)\delta(\mathbf{r}-\mathbf{r}') \\ &\quad + V(z,r) G^0_{Q\bar{Q}}(z) T_{Q\bar{Q}}(z,\mathbf{r},\mathbf{r}'). \end{aligned} \tag{41}$$

This is an algebraic equation with a solution $T_{Q\bar{Q}}(z,\mathbf{r},\mathbf{r}') = T_{Q\bar{Q}}(z,r)\delta(\mathbf{r}-\mathbf{r}')$ explicitly given by

$$T_{Q\bar{Q}}(z,r) = \frac{V(z,r)}{1-V(z,r)G^0_{Q\bar{Q}}(z)}. \tag{42}$$

We have factored out the δ function as was done in Eq. (37).[3] The Green function in frequency space in the static limit can be expressed as

$$G_{Q\bar{Q}}(z,r) = G^0_{Q\bar{Q}}(z) + G^0_{Q\bar{Q}}(z) T_{Q\bar{Q}}(z,r) G^0_{Q\bar{Q}}(z). \tag{43}$$

While in the nonstatic case, additional convolution integrals in coordinate space appear, the simple form in the static limit is due to the "$\delta(r)$" functions that can been integrated out (or stripped off). Upon inserting Eq. (42) into Eq. (43) we arrive at our final expression for $G_{Q\bar{Q}}$ in energy-coordinate space,

$$G_{Q\bar{Q}}(z,r) = \frac{1}{\left[G^0_{Q\bar{Q}}(z)\right]^{-1} - V(z,r)}. \tag{44}$$

[3]Only one δ function here is related to stripping off $\delta(\mathbf{p}_1+\mathbf{p}_2-\mathbf{p}'_1-\mathbf{p}'_2)$. Note that $X(\mathbf{p}_1-\mathbf{p}_2)\delta(\mathbf{p}_1+\mathbf{p}_2-\mathbf{p}'_1-\mathbf{p}'_2)$ Fourier transforms into the form $X(\mathbf{r}_1-\mathbf{r}_2)\delta(\mathbf{r}_1-\mathbf{r}'_1)\delta(\mathbf{r}_2-\mathbf{r}'_2)$.

To obtain $G^{>}(-i\tau,r)$, we need to transform back to imaginary time using $(-\beta)^{-1}\sum_n G_{Q\bar{Q}}(iE_n,r)e^{-\tau(iE_n)}$; employing a spectral representation and contour technique, the Matsubara sum can be carried out yielding

$$G^{>}_{Q\bar{Q}}(-i\tau,r) = \int_{-\infty}^{\infty} dE' \rho_{Q\bar{Q}}(E',r) \frac{e^{E'(\beta-\tau)}}{e^{\beta E'}-1}. \tag{45}$$

Since the strength of the two-particle spectral function, $\rho_{Q\bar{Q}}(E',r)$, is located in the vicinity of the large-mass two-particle threshold, $2M_Q$, we can approximate $e^{\beta E'}\gg 1$ and $e^{E'(\beta-\tau)}/(e^{\beta E'}-1) = e^{-E'\tau}$ to obtain

$$G^{>}_{Q\bar{Q}}(-i\tau,r) = \int_{-\infty}^{\infty} dE' \rho_{Q\bar{Q}}(E',r) e^{-E'\tau}. \tag{46}$$

The quantity $G^{>}(-i\tau,r)$ still depends on the infinitely large mass, M_Q (numerically taken as 2×10^4 GeV), which needs to be "renormalized." This can be done by multiplying $G^{>}(-i\tau,r)$ with a factor $e^{2M_Q\beta}$ and redefining the energy arguments of the propagators and spectral functions by a shift of $2M_Q$. For simplicity, we will keep the same notation, i.e., from here on, unless otherwise noted, the static limits of $G^{>}_{Q\bar{Q}}(-i\tau,r)$, $G_Q(z)$, $G_{Q\bar{Q}}(z)$, and $\rho_{Q\bar{Q}}(z)$ will refer to the original ones shifted as $G^{>}_{Q\bar{Q}}(-i\tau,r)e^{2\beta M_Q}$, $G_Q(z+M_Q)$, $G_{Q\bar{Q}}(z+2M_Q)$, and $\rho_{Q\bar{Q}}(z+2M_Q)$. Inserting Eqs. (44) and (46) into Eq. (38) with $\tau=\beta$ establishes our basic relation between the HQ potential and the free energy within the T-matrix formalism.

To be more explicit, we specify $[G^0_{Q\bar{Q}}(z)]^{-1}$ as

$$\left[G^0_{Q\bar{Q}}(z)\right]^{-1} = z - 2\Delta M_Q - \Sigma_{Q\bar{Q}}(z), \tag{47}$$

with medium-induced Fock mass term ΔM_Q (for each quark) determined by $V(r)$ as further discussed in Sec. III D, and an analytic self-energy part, $\Sigma_{Q\bar{Q}}(z)$, labeled as a two-body self-energy in this work. In practice, we can use $\mathrm{Im}[[G^0_{Q\bar{Q}}(E+i\epsilon)]^{-1}] = -\mathrm{Im}\Sigma_{Q\bar{Q}}(E+i\epsilon)$ to find the imaginary part and reconstruct $\mathrm{Re}\Sigma_{Q\bar{Q}}(E+i\epsilon)$ by a dispersion relation. The energy-dependent potential, $V(z,r)$, can also be decomposed into a static nonanalytic part, $V(r)$, and an analytic part, $V_A(z,r)$, so that $V(z,r)=V(r)+V_A(z,r)$. As elaborated in Appendix D, $V(r)$ is the input potential and $V_A(z,r)$ is related with interference effects induced by many-body physics, similar to $\Sigma_{Q\bar{Q}}(z)$. Therefore, we separate the input static potential $V(r)$ and regroup $V_A(z,r)$ into a "interfering" two-body self-energy as $\Sigma_{Q\bar{Q}}(z,r)\equiv\Sigma_{Q\bar{Q}}(z)+V_A(z,r)$ [note that $\Sigma_{Q\bar{Q}}(z,\infty)=\Sigma_{Q\bar{Q}}(z)$ since $V_A(z,\infty)=0$]; i.e.,

$$V(z,r) = V(r) + [\Sigma_{Q\bar{Q}}(z,r) - \Sigma_{Q\bar{Q}}(z)]. \tag{48}$$

Equation (44) can then be recast as

$$G_{Q\bar{Q}}(z,r) = \frac{1}{z-2\Delta M_Q - V(r) - \Sigma_{Q\bar{Q}}(z,r)}. \tag{49}$$

With this expression, $\Sigma_{Q\bar{Q}}(z,r)$ is analytic and $2\Delta M_Q+V(r)$ is a nonanalytic static part. In this scheme, the final compact

form for the free energy reads

$$F_{Q\bar{Q}}(r,\beta) = \frac{-1}{\beta}\ln\Bigg[\int_{-\infty}^{\infty} dE\, e^{-\beta E}\frac{-1}{\pi} \times \mathrm{Im}\Bigg[\frac{1}{E+i\epsilon-\tilde{V}(r)-\Sigma_{Q\bar{Q}}(E+i\epsilon,r)}\Bigg]\Bigg], \tag{50}$$

where $\tilde{V}(r) \equiv 2\Delta M_Q + V(r)$ is introduced for brevity.

2. Self-consistent extraction of the potential

To use Eq. (50) to extract the potential, $V(r)$, we need to evaluate $\Sigma_{Q\bar{Q}}(z,r)$. Toward this end, we first calculate the one-body self-energy, $\Sigma_Q(z)$. Taking the heavy-light T-matrix in Eq. (17) in the "half-static" limit where the $\mathbf{p}_1$ dependence in Eq. (10) is suppressed due to an infinite mass of particle-1, we obtain

$$\Sigma_Q(z) = \int\frac{d^3\mathbf{p}_2}{(2\pi)^3}\int_{-\infty}^{\infty} d\omega_2\frac{dE}{\pi}\frac{-1}{z+\omega_2-E}\frac{1}{d_Q}\sum_{a,j} d_s^{Qj} d_a^{Qj} \times T^a_{Qj}(E,\mathbf{p}_2|\mathbf{p}_2)\rho_j(\nu,\mathbf{p}_2)n_j(\nu). \tag{51}$$

The CM transformation in the static limit, $\omega_1+\omega_2 \gg |\mathbf{p}_1+\mathbf{p}_2|$, can be derived as

$$E_{\mathrm{cm}} = \omega_1+\omega_2, \quad p_{\mathrm{cm}} = p_2, \quad \cos(\theta_{\mathrm{cm}}) = \cos(\theta). \tag{52}$$

The n_{ij} is suppressed due to infinite mass of two-body states. The self-consistent Eq. (19) also applies in the static limit. For the two-body self-energy, $\Sigma_{Q\bar{Q}}(z)$, we first use Eq. (39) to obtain the two-body propagator, $G^0_{Q\bar{Q}}(z)$, and then use the procedure laid out after Eq. (47) to arrive at $\Sigma_{Q\bar{Q}}(z)$.

In the Brueckner type setup of our approach, the r-dependent part of the two-body "interfering" self-energy, $\Sigma_{Q\bar{Q}}(z,r)$, is not self-consistently generated, as this would require to include 3-body interactions.[4] For now, we model $\Sigma_{Q\bar{Q}}(z,r)$ with a factorizable ansatz,

$$\Sigma_{Q\bar{Q}}(z,r) = \Sigma_{Q\bar{Q}}(z,\infty)\phi(x_e r) \equiv \Sigma_{Q\bar{Q}}(z)\phi(x_e r), \tag{53}$$

which preserves the analyticity of $\Sigma_{Q\bar{Q}}(z,r)$. The function $\phi(x_e r)$ is motivated by the imaginary part of the potential in a perturbative approximation [59,60] and will be constrained in our context by a functional fit (within its short- and long-distance limits of one and zero, respectively). Here, x_e is a dimensionless parameter acting as a screening mass that shrinks the range of $\phi(x_e r)$ as temperature increase (our pivot point at the lowest temperature considered here is set to $x_e = 1$). Inserting Eq. (53) into Eq. (50) gives

$$F_{Q\bar{Q}}(r,\beta) = \frac{-1}{\beta}\ln\Bigg[\int_{-\infty}^{\infty} dE\, e^{-\beta E}\frac{-1}{\pi} \times \mathrm{Im}\Bigg[\frac{1}{E+i\epsilon-\tilde{V}(r)-\Sigma_{Q\bar{Q}}(E+i\epsilon)\phi(x_e r)}\Bigg]\Bigg], \tag{54}$$

where the input functions $V(r)$ and $\phi(x_e r)$ are to be tuned to reproduce lQCD data. In our previous work [17], $\Sigma_{Q\bar{Q}}(E+i\epsilon)$ was modeled by a functional ansatz with few parameters and as such was the major source of the uncertainties in the approach. In the present work, $\Sigma_{Q\bar{Q}}(E+i\epsilon)$ is controlled self-consistently by the single heavy-quark/antiquark self-energy, $\Sigma_Q/\Sigma_{\bar{Q}}$, as outlined above.

C. Quarkonium correlator ratios

The Euclidean correlator can be understood as "Fourier transform" of the spectral function to imaginary-time space, where it is computable in lattice QCD. Its ratio to correlator with a vacuum reference function is utilized to highlight the medium modifications in the spectral functions, and it also has the advantage of reducing systematic lattice uncertainties. Since the quarkonium correlator is defined by a local operator, the two-body Green function/spectral function is proportional to the wave function overlap at the origin, $G_{ij}(E) = \sum_n |\phi_{E_n}(0)|^2/(E-E_n)$. Thus, the correlator is quite sensitive to short-range physics, which is useful to, e.g., constrain the strong coupling constant α_s in the Coulomb term. The spectral function and the correlator can be readily calculated in the T-matrix approach with heavy quarks. There are several previous studies of these quantities in this approach [11,13,14] which we will briefly review. Here, we are now able to significantly go beyond those by consistently coupling the heavy quarks to an off-shell light-parton plasma.

1. Review of established formalism

The correlator in the Euclidean time that can be computed in lQCD [49–51] is defined by

$$G^{>}(-i\tau,\mathbf{P}) = \int d^3\mathbf{r}\, e^{i\mathbf{P}\cdot\mathbf{r}}\langle J_M(-i\tau,\mathbf{r}), J_M^{\dagger}(0,0)\rangle \tag{55}$$

and usually evaluated at vanishing total 3-momentum, $\mathbf{P}$, of the $Q\bar{Q}$ pair,

$$G^{>}(-i\tau) \equiv G^{>}(-i\tau,\mathbf{P})|_{P=0}. \tag{56}$$

The mesonic states are created by the local operator

$$J_M(-i\tau,\mathbf{r}) = \bar{\psi}(t,\mathbf{r})\Gamma_M\psi(t,\mathbf{r}), \tag{57}$$

where ψ ($\bar{\psi}$) denotes the (conjugate) Dirac spinor field operator. The Dirac matrix $\Gamma_M \in \{1,\gamma_\mu,\gamma_5,\gamma_\mu\gamma_5\}$ projects the operators into scalar, vector, pseudoscalar, and pseudovector channels, respectively. In a fully relativistic treatment, ψ can create an antiparticle or annihilate a particle. However, in the context of this paper, we separately treat particle annihilation and antiparticle creation (and vice versa) by two field operators ψ_Q and $\psi^{\dagger}_{\bar{Q}}$, respectively, schematically written as $\psi = \psi_Q + \psi^{\dagger}_{\bar{Q}}$ (here and in the following, we also use Q to denote c and b quarks). Inserting this into Eqs. (57) and (55) (suppressing the Γ_M structure and pertinent relativistic corrections), a leading term of the 16 possibilities for this correlator is the 4-point

[4] Ideas to self-consistently generate this part are presented in Appendix III C 2.

Green function

$$G^{>}_{Q\bar{Q}}(-i\tau,\mathbf{P}) = \int d^3\mathbf{r}\, e^{i\mathbf{P}\cdot\mathbf{r}} G^{>}_{Q\bar{Q}}(-i\tau,\mathbf{r},\mathbf{r}|0,0)$$
$$= \int d^3\mathbf{r}\, e^{i\mathbf{p}\cdot\mathbf{r}} \langle \psi_{\bar{Q}}(-i\tau,\mathbf{r})\psi_Q(-i\tau,\mathbf{r})$$
$$\times \psi^\dagger_Q(0,0)\psi^\dagger_{\bar{Q}}(0,0)\rangle, \quad (58)$$

which characterizes the propagation of a two-body state and can be solved by the T-matrix as shown in the previous section. Another important term for the same correlator is the density-density correlation function,

$$\langle n_Q(-i\tau,\mathbf{r}) n_Q(0,0)\rangle$$
$$= \langle \psi^\dagger_Q(-i\tau,\mathbf{r})\psi_Q(-i\tau,\mathbf{r})\psi^\dagger_Q(0,0)\psi_Q(0,0)\rangle, \quad (59)$$

which is usually referred to as the zero-mode contribution (or Landau cut) and closely related to the transport properties of the medium [14]. Other terms are either included automatically through the Matsubara formalism as hole excitations, or they are suppressed in the HQ limit. For the purpose of this paper, we choose the simplest quantity to be compared with lQCD data, i.e., the pseudoscalar channel, $\Gamma_M = \gamma_5$, which does not develop a zero mode. It corresponds to the mesonic η_c and η_b channels (including, of course, their full excitation spectrum).

Since we focus on the Euclidean time correlator at total momentum $\mathbf{P} = 0$, it simply corresponds to the T-matrix in the CM frame. The additional locality in the relative coordinate leads to one integration over 3-momentum.[5] Thus, the 4-point Green function in frequency space for the pseudoscalar channel takes the form

$$G_{Q\bar{Q}}(z) = d_Q \int \frac{d^3p}{(2\pi^3)} G^0_{Q\bar{Q}}(z,p)$$
$$+ d_Q \int \frac{dpdp'}{\pi^3} \mathcal{R}^{\mathcal{S}}_{Q\bar{Q}} G^0_{Q\bar{Q}}(z,p) T^I_{Q\bar{Q}}(z,p,p')$$
$$\times G^0_{Q\bar{Q}}(z,p'). \quad (60)$$

It includes the relativistic effects due to the projector Γ_M, encoded in the $\mathcal{R}^{\mathcal{S}}_{ij}$ defined in Eqs. (2), (3), and (4), cf. Refs. [11,13,14] for more details (in those works the $\mathcal{R}$ factor is part of the propagator, but the expressions are equivalent to the ones used here); $d_Q = 6$ denotes the spin-color degeneracy of a heavy quark. The spectral function for this Green function is defined as

$$\rho_{Q\bar{Q}}(E,T) = -\frac{1}{\pi}\mathrm{Im}G_{Q\bar{Q}}(E+i\epsilon), \quad (61)$$

and the pertinent correlator is given by

$$G^{>}_{Q\bar{Q}}(-i\tau,T_{\rm ref},T) = \int_0^\infty dE \rho_{Q\bar{Q}}(E,T_{\rm ref})\mathcal{K}(\tau,E,T), \quad (62)$$

with the kernel

$$\mathcal{K}(\tau,E,T) = \frac{\cosh[E(\tau-\beta/2)]}{\sinh[E(\beta/2)]}, \quad (63)$$

which can be obtained using the contour techniques with proper treatment of the retarded symmetry for spectral function for negative E. Finally, the correlator ratio is defined as

$$R_{Q\bar{Q}}(\tau,T_{\rm ref},T) = \frac{G^{>}_{Q\bar{Q}}(-i\tau,T,T)}{G^{>}_{Q\bar{Q}}(-i\tau,T_{\rm ref},T)}. \quad (64)$$

In this ratio the denominator and the numerator carry the exact same kernel, $\mathcal{K}(\tau,E,T)$, so that the only difference is the spectral function, thus exhibiting the medium effects relative to a reference spectral function (usually taken as one at small temperature).

2. *Interference effect for two-body spectral function*

As discussed in Appendix D, the r-dependent imaginary part of the potential is a manifestation of interference effects between the two quarks when interacting with the medium; e.g., in the singlet channel a small size $Q\bar{Q}$ state will effectively become colorless thus suppressing any interaction with the colored medium partons. Therefore, this effect is expected to become significant for deeply bound heavy quarkonia with a tight wave function. Although a full many-body treatment will require nontrivial 3-body diagrams, we will suggest a way to include the effects in the T-matrix approach, which seems viable for the case of two-body spectral functions and correlators. However, we will only include the interference effects for heavy-heavy and static-static channels.

We start from the nonrelativistic Schrödinger equation,

$$\left[-\frac{\partial_r^2}{M} + \tilde{V}_{\rm clx}(r)\right]\varphi(r) = E\varphi(r). \quad (65)$$

In previous works [60,61], an energy-independent complex "potential" has been introduced; in our context we write it as $\tilde{V}_{\rm clx}(r) = V(r) + i\Sigma^I_{Q\bar{Q}}\phi(x_e r)$, where we introduced the generic notation $\Sigma^I \equiv \mathrm{Im}\Sigma$. Transforming it to momentum space leads to

$$\tilde{V}_{\rm clx}(\mathbf{p}-\mathbf{p}') = i\Sigma^I_{Q\bar{Q}}(2\pi)^3\delta(\mathbf{p}-\mathbf{p}')$$
$$+ i\Sigma^I_{Q\bar{Q}}\phi_N(\mathbf{p}-\mathbf{p}') + V(\mathbf{p}-\mathbf{p}'), \quad (66)$$

where $\phi_N(\mathbf{p}-\mathbf{p}')$ is the Fourier transform of $\phi(x_e r) - 1$,

$$\phi_N(p) = \int d^3\mathbf{r}\, e^{i\mathbf{p}\cdot\mathbf{r}}[\phi(x_e r) - 1]. \quad (67)$$

The Schrödinger equation in momentum space then reads

$$\int \frac{d^3\mathbf{p}'}{(2\pi)^3}\left\{\left[\frac{p^2}{M} + i\Sigma^I_{Q\bar{Q}}\right](2\pi)^3\delta(\mathbf{p}-\mathbf{p}')\right.$$
$$\left. + i\Sigma^I_{Q\bar{Q}}\phi_N(\mathbf{p}-\mathbf{p}') + V(\mathbf{p}-\mathbf{p}')\right\}\varphi(\mathbf{p}') = E\varphi(\mathbf{p}). \quad (68)$$

One can now follow the standard track to derive the Lippmann-Schwinger equation (LSE). The terms in the brackets "[ ]" figure in H_0, which is combined with E on the right-hand side as $(E - H_0)\varphi = V\varphi$. Then, inverting the left-hand side and adding a free solution, we obtain the general solution as $\varphi = \varphi_0 + (E - H_0 + i\epsilon)^{-1}V\varphi$. Multiplying it by V, we arrive at the T-matrix equation $T = V + (E - H_0 + i\epsilon)^{-1}VT$ using $V\phi = T\phi_0$. The part local in momentum with a δ function in

[5] $f(\mathbf{r}_1-\mathbf{r}_2) = \int \frac{d^3\mathbf{p}}{(2\pi)^3} e^{i\mathbf{p}\cdot(\mathbf{r}_1-\mathbf{r}_2)} f(p) \to f(0) = \int \frac{d^3\mathbf{p}}{(2\pi)^3} f(p)$.

Eq. (66) enters the free propagator, while the part nonlocal in momentum space becomes the true potential.

To generalize the Schrödinger framework to be compatible with the T-matrix approach discussed in previous sections (in particular in Sec. III B 1), a few extensions are required. Specifically, the energy-momentum dependence and analytic properties of the uncorrelated in-medium two-particle propagator need to be accounted for. Toward this end, motivated by the relation Eq. (47) in the static limit, we augment the constant imaginary part to an energy-dependent complex quantity, $\Sigma_{Q\bar{Q}}(z,p)$, whose local part (with a 3-momentum δ function) encodes the dynamical single-quark self-energies, while its nonlocal part accounts for interference effects (as a coefficient to the "interference" function, ϕ),

$$\tilde{V}_{\rm clx}(z,\mathbf{p}-\mathbf{p}') = (2\pi)^3\delta(\mathbf{p}-\mathbf{p}')\Sigma_{Q\bar{Q}}(z,p) + \Sigma_{Q\bar{Q}}(z,p')\phi_N(\mathbf{p}-\mathbf{p}') + V(\mathbf{p}-\mathbf{p}'). \quad (69)$$

Thus, the modified potential figuring as a kernel in the T-matrix equation takes the form

$$V_{\rm clx}(\mathbf{p}-\mathbf{p}') = \Sigma_{Q\bar{Q}}(z,p')\phi_N(\mathbf{p}-\mathbf{p}') + V(\mathbf{p}-\mathbf{p}'), \quad (70)$$

which is then subjected to a standard partial-wave expansion. The resulting spectral function does not depend on using $\Sigma_{Q\bar{Q}}(z,p)$ or $\Sigma_{Q\bar{Q}}(z,p')$ in the above equation since ϕ_N is symmetric under the exchange of $\mathbf{p}$ and $\mathbf{p}'$. With this setup, the T-matrix is still analytic but no longer positive-definite. The latter feature causes complications when utilized in many-body calculations of single-particle self-energies. It is indicative of a nonconserving approximation [19]. However, when restricted to the calculation of the quarkonium spectral functions and correlators, the former remains strictly positive definite. In addition, this scheme precisely recovers the implementation of V_I in the static limit. In Sec. IV, we will elaborate on the interference effects for the spectral functions obtained from this implementation.

D. Potential ansatz and numerical procedure

1. Screened Cornell potential and bare parton masses

For the Hamiltonian introduced in Eq. (1), the inputs are the two-body potential and bare particle masses which both depend on temperature. As an ansatz for the potential, we employ a generalized in-medium Cornell potential [62,63],

$$V(r) = V_{\mathcal{C}} + V_{\mathcal{S}} = -\frac{4}{3}\alpha_s\frac{e^{-m_d r}}{r} - \frac{\sigma e^{-m_s r-(c_b m_s r)^2}}{m_s}, \quad (71)$$

which recovers the well-established vacuum form while implementing in-medium screening of both the shot-range Coulomb and long-range confining interaction ("string term") in a transparent and economic way. The respective screening masses are denoted by m_d and m_s. An additional quadratic term, $-(c_b m_s r)^2$, in the exponential factor of the string term accelerates the suppression of the long-range part, mimicking a string-breaking feature. It can also be considered as the next term in a power expansion in r.

Since the screening originates from the coupling of the bare interaction to medium partons, both m_s and m_d are functions of the parton density and thus they are not totally independent. The $1/r$ and r dependence of the potential leads to static propagators in momentum space, $D_c(q) = 1/q^2$ and $D_s = 1/q^4$, respectively, which, upon multiplication with the respective coupling constants, $-4/3\alpha_s$ and $-8\pi\sigma$ in singlet channel, constitutes the bare potential in the Hamiltonian. The screening effects at leading order can therefore be expected to be of a generic form,

$$D_c(r) = \frac{1}{p^2 + A\alpha_s\Pi}, \quad (72)$$

$$D_s(r) = \frac{1}{p^4 + B\sigma\Pi}, \quad (73)$$

with a medium-induced polarization tensor Π representing light-parton loops,[6] which are only related with medium properties. Thus, they are the same for Coulomb and string terms. However, the same Π can lead to different screening behavior since Coulomb and string potentials couple to Π differently. Here, we simply assume that this difference can be represented by temperature-independent parameters A and B related to spin/color and relativistic structures which are not precisely known in our context. From dimensional analysis a "propagator" of the form $1/(p^n + m_x^n) = m_x^{-n}/[(p/m_x)^n + 1]$ has a screening mass proportional to m_x. Thus, we have $m_d \propto (A\alpha_s\Pi)^{1/2}$ and $m_s \propto (B\sigma\Pi)^{1/4}$. This yields the constraint $m_s = (c_s m_d^2\sigma/\alpha_s)^{1/4}$ where c_s is depending on A and B and other temperature-independent constants. In a Debye-Hückel approach [61] one obtains the same temperature scaling relation for string and Debye masses except for the coefficient c_s. However, the resulting screening behavior of the above model and the Debye-Hückel approach can be different. Thus, we do not directly use the above propagators or the Debye-Hückel approach as our ansatz but simply use scaling rules with c_s as a parameter for the Coulomb or string screening masses, which show indications of model independence. The above potential is in the quark-antiquark color-singlet channel, while the potentials in other channels will be modified by Eqs. (3) and (4) and Table. I.

In our fit procedure, we first constrain the infinite-distance limit of the input potential $V(r)$ by using $F_{Q\bar{Q}}(\infty,\beta)$ (they are not the same). Then, the "interference function", $\phi(x_e r)$ defined Eq. (53), is constrained via Eq. (54), which is a functional fit. The solution for $\phi(x_e r)$ is unique once $V(r)$ is fixed (it will turn out to have a shape similar to the perturbative limit in Ref. [60], as will be shown in Figs. 3 and 8, in Secs. IV A 1 and IV B 1).

For the quark mass correction, we have previously defined $\tilde{V}(r)$ by adding twice the Fock term, $\Delta M_Q = \tilde{V}(\infty)/2$, to the genuine interaction part of $V(r)$, i.e.,

$$\tilde{V}(r) = V_{\mathcal{C}}(r) + V_{\mathcal{S}}(r) + 2\Delta M_Q, \quad (74)$$

where

$$\Delta M_Q = -\frac{1}{2}\int dr\rho(r)V(r) = \frac{1}{2}\left(-\frac{4}{3}\alpha_s m_d + \sigma m_s\right) \quad (75)$$

is the classical static in-medium self-energy of a point charge, $\rho(r) = \delta(r)$, in its own field, subtracting the divergent vacuum

[6]The leading-order polarization is just a particle-hole loop.

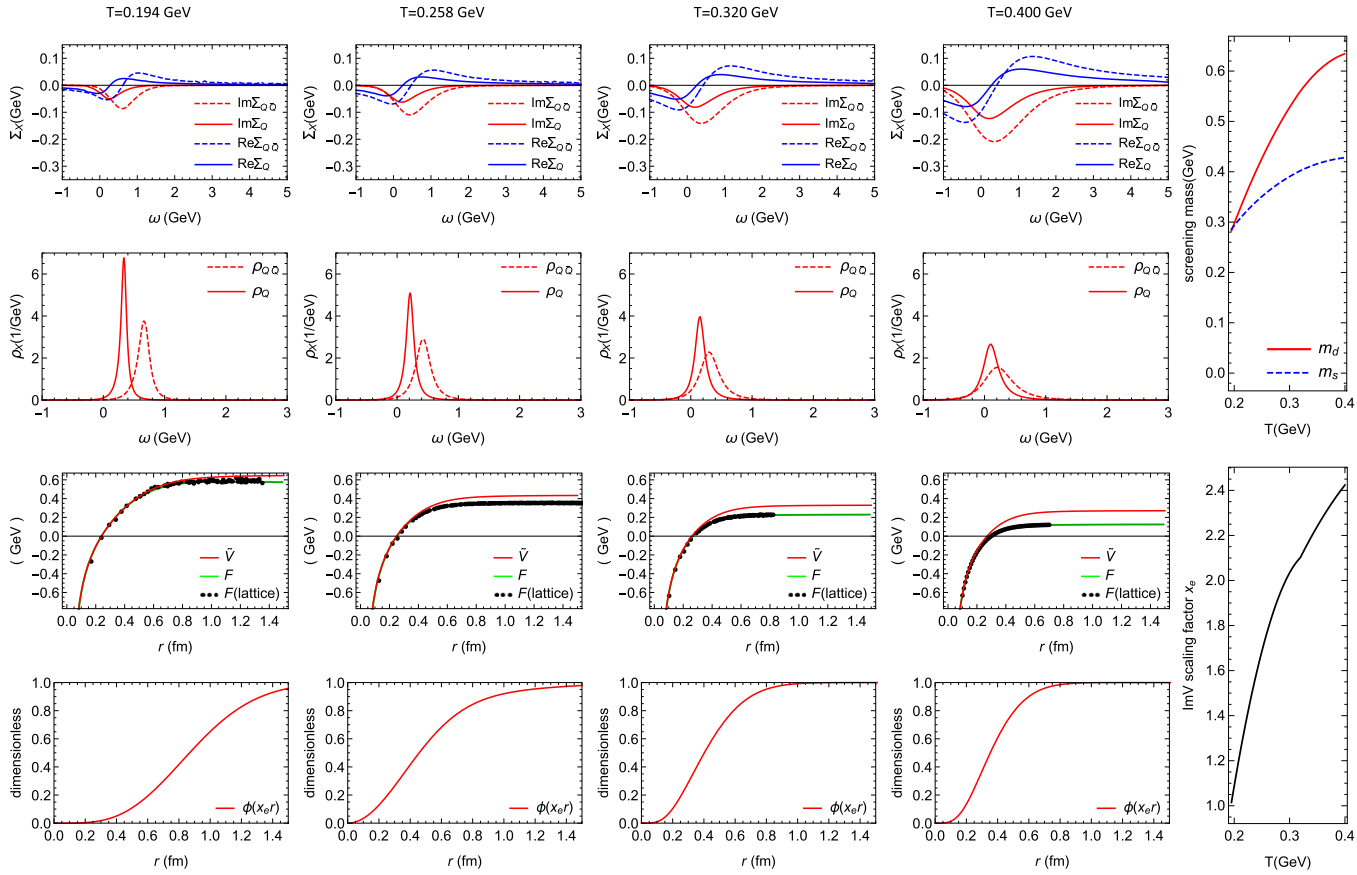

FIG. 3. Results of a *weakly* coupled solution for the self-consistent fit to extract the static HQ potential: single HQ and $Q\bar{Q}$ self-energies, $\Sigma_X(\omega,\infty)$ (first row), and spectral functions, $\rho_X(z,\infty)$ (second row), potential $\tilde{V}(r)$ and free energies (third row), and interference function, $\phi(x_e r)$ (fourth row), in the first four columns corresponding to different temperatures. The last column shows the temperature dependence of the fitted screening masses (top panel) and the scale factor, x_e (bottom panel), figuring in the interference function. The free-energy lQCD data are from Ref. [48].

term. The minus sign arises because the charge repels itself. Similar physics is discussed in Ref. [64] in the perturbative context. Using Eq. (75) in momentum space with explicit indices, the Fock mass can be obtained by the self-energy from a potential including the relativistic and color factors, Eqs. (3) and (4),

$$M_q = -\frac{1}{2}\int \frac{d^3\mathbf{p}}{(2\pi)^3} V^1_{q\bar{q}}(\mathbf{p}) + M_{\rm fit},$$
$$M_g = -\frac{1}{2}\int \frac{d^3\mathbf{p}}{(2\pi)^3} V^1_{gg}(\mathbf{p}) + \frac{3}{2}M_{\rm fit}, \tag{76}$$

where $M_{\rm fit}$ is a residual mass (utilized as a fit parameter to the lQCD data for the EoS), which encodes physics that we do not treat explicitly here (e.g., perturbative self-energies or gluon condensate effects).[7] The nonperturbative gluon-quark mass ratio in the static limit is $M_g/M_q = C_A/C_F = 9/4$, while in the perturbative limit at high T one has $M_g/M_q = 3/2$. The above implementation gives a smooth transition from the nonperturbative to the perturbative regime. However, the mass dependence in the relativistic factor still requires a self-consistent procedure. We have checked that our default the mass fitting scheme, using Eq. (76), and the scheme described in the footnote below, give very similar results, with a maximum difference of 1% for the resulting quark masses, up to 15% for the gluon masses, 10% for the self-energy near $T \approx 0.2$ GeV, and at the 5% level for gluon masses and self-energies at $T \approx 0.3$ GeV. In either case the influence on the emerging spectral properties is not significant. Preliminary results show that the quark-number susceptibilities are rather sensitive to the masses and can provide additional constraints; this will be elaborated in future work.

2. *Numerical fit procedure for lQCD data*

Let us briefly lay out the numerical procedure we use to search for solutions of our approach that are compatible with the lQCD data for the QGP EoS, quarkonium correlators and static $Q\bar{Q}$ free energies. At each temperature, we start with trial values for the potential and two light parton masses, and we use them to calculate the nonperturbative off-shell scattering matrices (T-matrices) for light partons. Within the formalism laid out in Sec. II, we keep six partial waves to include two-body channels with angular momentum up to $l = 5$ (which is

[7]Neglecting the relativistic factor in Eq. (76), the relation is $M_q = \frac{\tilde{V}(\infty)}{2} + M_{\rm fit}, M_g = \frac{9}{4}\frac{\tilde{V}(\infty)}{2} + \frac{3}{2}M_{\rm fit}$.

more than sufficient for convergence); with four color channels in the qq and $q\bar{q}$, three in the qg and three in the gg sector [9], a total of $6 \times 10 = 60$ different light-parton T-matrices are computed. These T-matrices are then used to calculate the self-energies and spectral functions for single partons. Next, the parton propagators are reinserted back into the T-matrices, forming a self-consistency problem [recall Eq. (19)], which is solved by numerical iteration; this forms the "inner" light-parton self-consistency loop of the overall procedure. The pertinent outputs are then used to compute the EoS and LWF as discussed in Sec. III A. If the resulting pressure disagrees with the lQCD value at the given temperature, the light-parton masses ($M_{\rm fit}$) are retuned, the inner self-consistency loop carried out, and repeated until the EoS is reproduced, constituting the "intermediate" mass fitting loop of the overall procedure. After obtaining the masses to reproduce the lQCD EoS, we proceed to the self-consistent calculation of the self-energy of a static quark (again a self-consistency loop), which involves another 42 static-light T-matrices (six partial waves and a total of seven color channels for Qq, $Q\bar{q}$, and Qg). These are input to the formalism laid out in Sec. III B to compute the static-quark free energy, $F_{Q\bar{Q}}$, and compare it to pertinent lQCD data. If the calculated free energy disagrees with the lQCD data, we retune the potential (most notably m_d), recalculate the EoS with retuned light-parton masses, and recompute the free energy, which corresponds the "outer" potential fitting loop of the procedure. These loops involve automated (numerical) adjustments of $M_{\rm fit}$ and m_d to best reproduce the EoS and free-energy data while other parameters are tuned manually. After obtaining a solution, we proceed to the self-consistent calculations of charm- and bottom-quark properties which involve another 42 heavy-light T matrices each. With the full off-shell HQ spectral functions, we proceed to evaluate two more T-matrices to compute charmonium and bottomonium spectral functions and correlator ratios in the pseudoscalar color-singlet S-wave channel, and compare the latter to lQCD data as discussed in Sec. III C. If they do not match, we manually retune the potential (mostly the Coulomb term) and redo the whole process until a satisfactory result is obtained. Usually, the fits to the correlator ratio are automatically "satisfactory" with the assumption that α_s does not strongly depend on temperature. The numerical machinery is carried out with *Mathematica* software and typically takes several hundreds of CPU hours to arrive at a solution at four temperatures.

IV. SELFCONSISTENT NUMERICAL RESULTS

In this section, we discuss the results and insights from the above framework. For each solution at a given temperature, all quantities in both HQ and light-parton sectors, i.e., the QGP EoS, free energy, one- and two-body spectral functions, and T-matrices are all calculated from a single Hamiltonian, Eq. (1), with the potential ansatz described in Sec. III D, and then using the T-matrix approach with one set of parameters. The interference effect discussed in Sec. III C 2 is only included when evaluating static-static and heavy-heavy spectral functions and correlators/free energies.

As it turns out, the constraints provided by the currently used set of lQCD data (free energies, quarkonium correlators, and EoS) does not yet allow for a unique solution. To explore this feature, we will focus on two putatively limiting cases, which we denote by a weakly coupled solution (WCS) where the potential is close to the free energy (Sec. IV A) and which has already been discussed in the literature in perturbatively inspired frameworks [16,59,61], and a strongly coupled solution (SCS), which is characterized by a long-range potential which "maximally" rises above the free energy (Sec. IV B), first pointed out in Ref. [17]. Although both solutions can explain the chosen set of lQCD data, they predict, as we will see, a rather different microscopic structure of the QGP at moderate temperatures.

A similar discussion has been presented before in phenomenological applications heavy-flavor observables, both for HQ diffusion [13,65] and quarkonium transport [66–69]. In these instances the internal and free energies have been employed as potential proxies for strongly and weakly coupled scenarios of the in-medium QCD force. A general tendency for preferring the internal energy was found. Such studies can, of course be repeated with our more rigorously deduced potential solutions.

One of the virtues of our approach is that it is carried out in real-time, allowing us to retain and keep track of the microscopic quantum many-body information about the system in a direct way while being intimately connected to the macroscopic properties of the QGP. This includes the predicted spectral functions of all involved partons (static, heavy and light quarks as well as gluons) and the more than one-hundred in-medium two-body T-matrices, fully off-shell. This information readily allows to calculate transport coefficients, Wigner functions for one- or two-body states, etc., in a nonperturbative framework, and to make contact with experimental observables. Thus, the approach is not only rooted in lQCD data, but also unravels real-time microscopic physics which predicts a wide variety of phenomena that can be tested by experiments in a transparent, quantitative and interpretable way.

A. Weakly coupled solution

In this section we first report and discuss the results of our fits for a weakly coupled solution (WCS), starting from the HQ free energy and the extraction of the underlying potential, which is the key quantity determining the interaction strength in the QGP (Sec. IV A 1) and pivotal for calculating essentially all other quantities. In Sec. IV A 2 we elucidate the extra information that can be gained by the fits of Euclidean quarkonium correlators, and we discuss the resulting charmonium and bottomonium spectral functions. We then proceed to our fit to the QGP EoS, which involves the two light-parton masses as additional fit parameters (Sec. IV A 3). We finally give a comprehensive overview of the emerging light and heavy-parton spectral functions and their two-body T matrices (Sec. IV A 4) and a discussion of the pertinent QGP structure, including its degrees of freedom.

1. Free energy, potential, and static self-energies

When searching for a WCS, we start by using the free energy as potential. The strength of the potential slightly increases in the iteration procedure, mostly due to relatively

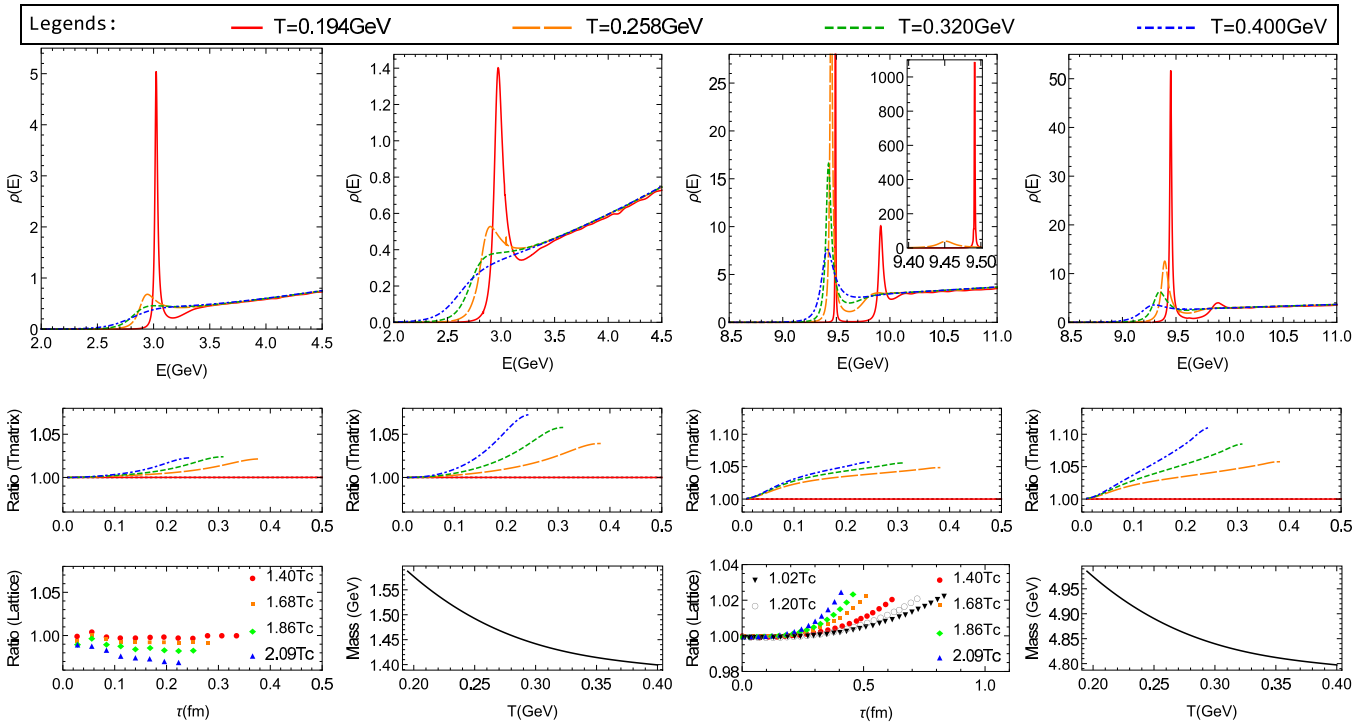

FIG. 4. *Weakly* coupled solution for charmonium (η_c, left panels) and bottomonium (η_b, right panels) spectral functions (upper panels) and correlators ratios (middle panels) with (first and third column) and without (second and fourth column) interference effects in the imaginary part of the potential. The lQCD data for η_c [51] and η_b [52] correlator ratios are shown in the first and third bottom panel, respectively, while the second and fourth bottom panel display the temperature dependence of the charm- and bottom-quark mass, respectively.

small imaginary parts that develop and figure in the static $Q\bar{Q}$ spectral function, Eq. (54). Thus, the solution found in this way can be regarded as a lower limit of the potential. The parameters of the potential for the converged solution are given by $\alpha_s = 0.27$, $\sigma = 0.21$ GeV^2, $c_b = 1.3$ and a temperature dependent Coulomb Debye mass, m_d, as shown in the upper right panel of Fig. 3. With $c_s = 0.1$ the screening mass of the string term, $m_s = (c_s m_d^2 \sigma/\alpha_s)^{1/4}$, also follows as shown in the same panel. The fit of the interference function, shown in the lowest row of Fig. 3, is quite similar to the perturbative function found in Ref. [60]; it shrinks in range as a result of the increase in screening with temperature. The resulting potential is displayed in the third row of Fig. 3 and indeed found to exceed the free energy, by up to 0.07 GeV at $T = 0.194$ GeV and 0.16 GeV at $T = 0.4$ GeV. The calculated free energy fits the lQCD data well.

With this potential, the self-consistent self-energy and spectral function of a static quark follow from T-matrix approach as shown in the first two rows of Fig. 3, respectively. In practice, the static limit has been calculated with a numerically large bare HQ mass (2×10^4 GeV), and the energy scales for the one- (and two-) body quantities have been plotted relative to (twice) that bare mass. At low $T = 0.194$ GeV, the peak value of $\mathrm{Im}\Sigma_Q \approx -0.05$ GeV corresponds to a width of the spectral function which is around 0.1 GeV. For comparison, the hard-thermal-loop (HTL) perturbative width [59,60,64] is $\frac{4}{3}\alpha_s T \approx 0.07$GeV. For the $Q\bar{Q}$ quantities, the peak value of $\mathrm{Im}\Sigma_{Q\bar{Q}}$ as defined in Eqs. (47) and (53) is approximately two times of the peak value of $\mathrm{Im}\Sigma_Q$, and the width of the two-body spectral function is around two times that of the single static-quark spectral function. The peak value of $\mathrm{Im}\Sigma_Q$ and the width of the static quark spectral functions increase with temperature at an approximately linear rate.

2. *Quarkonium correlators and spectral functions*

Next we turn to the Euclidean quarkonium correlators for realistic bottom- and charm-quark masses, concentrating on the pseudoscalar channel where extra complications due to zero modes do not figure; see Fig. 4. The bare masses of charm and bottom quarks (Q=c,b) are determined as in Ref. [13], by fitting the vacuum charmonium and bottomonium ground-state masses using $m_Q = m_Q^{\mathrm{bare}} + \tilde{V}(\infty)/2$ with the vacuum value of $\tilde{V}$ at a typical string breaking scale of r=1-1.1 fm, resulting in $m_{c,b}^{\mathrm{bare}}$=1.264, 4.662 GeV.

The widths of the quarkonium spectral functions are caused by collisions of individual heavy quarks within the bound state with medium partons (the so-called quasifree process [70]), as encoded in the HQ self-energies. Since the potential is relatively weak, these self-energies are small, and so is the width of quarkonium. The η_c is still a well-defined state at $T = 200$ MeV, but is essentially dissolved at $T = 260$ MeV. The $\eta_b(1S)$ survives to significantly higher temperatures, beyond 260 MeV, and even to 400 MeV when interference effects are included (as described in Sec. III C 2). The latter generally reduce the quarkonium widths, more so the tighter the states are bound (by up to 75%). The width reduction is consistent with simple estimates using the $\phi(x_e r)$ function (Fig. 3) with pertinent size estimates. Even for the case without

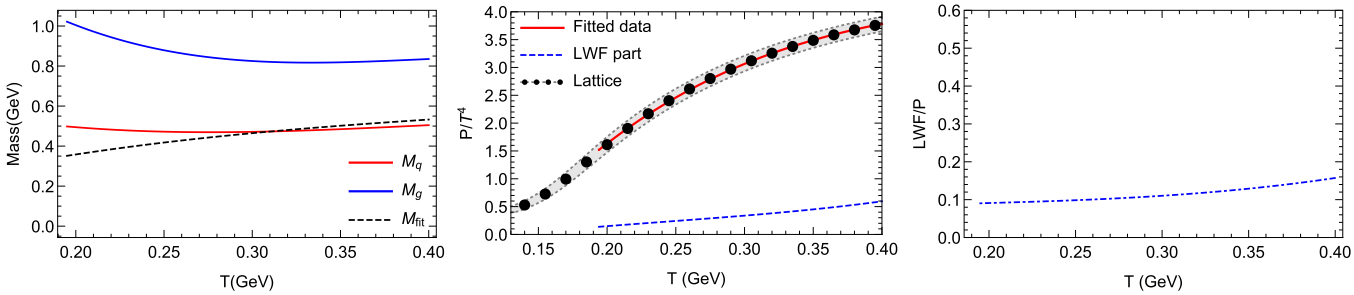

FIG. 5. *Weakly* coupled solution for the QGP bulk medium: fit results for the input masses for quarks and gluons (left panel), the QGP pressure in comparison to lQCD data [46] (middle panel; solid line: total, dashed line: LWF contribution), and the ratio of LWF contribution to total pressure (right panel).

interference, the width of the $Q\bar{Q}$ states is smaller than two times the HQ width at vanishing momentum, due to the energy-momentum dependence of the HQ self-energies as obtained from the heavy-light T-matrices. As usual, the dissolution of the quarkonia is due to a combination of the increasing screening and collision widths.

The correlator ratios are generated by using the reference (or "reconstructed") correlator at the lowest temperature considered ($T = 194$ MeV), as was done in the lQCD calculations that we compare to Refs. [51,52]. Without interference effects the calculated correlator ratios deviate from the lQCD data by up to $\sim$10%. Despite the melting of the bound states, the increase in width effects (over-) compensates the loss of low-energy strength in the spectral functions and leads to a 5–10% increase in the correlators ratios with increasing Euclidean time, τ. This increase is tamed by the inclusion of interference effects, which, as discussed above, reduce the bound-state widths; the resulting correlator ratios agree within $\sim$5% with the lQCD data. Furthermore, the correlator ratios are quite sensitive to the strong coupling constant, α_s (approximately proportional to it, reflecting its short distance nature as a local operator related to the wave function overlap at the origin (recall the discussion in Sec. III C). Thus, the deviations between our results and the lQCD data could be further mitigated by a fine-tuning of α_s, slightly decreasing with temperature at a few-percent level. In our fits we did not explore such a dependence, given other uncertainties that can affect the correlator ratios at a similar level (e.g., spin-dependent interactions). In turn, one could argue that the fact that the lQCD correlator ratios are quite close to 1 at all temperatures suggest that α_s is not strongly running with temperature.

3. QGP equation of state

Next, we turn to the self-consistent results for the QGP bulk properties, i.e., our fit to the lQCD data for the pressure. Here, the two main fit parameters are the bare light-parton masses in the Hamiltonian [including the Fock term, recall Eq. (76)], which are shown in the left panel of Fig. 5. The resulting masses are rather stable with temperature, with a slight increase toward $T_{\rm pc}$ dictated by the decreasing pressure (not unlike in quasiparticle models, but less pronounced, especially for quarks). The quark-to-gluon mass ratio is different from the perturbative thermal mass ratio due to the nonperturbative ingredients of the interaction as discussed in Sec. III D. The fitted mass parameter, $M_{\rm fit}$, starts to exceed M_q for temperatures above 300 MeV due the negative Coulomb contribution to the Fock term (which is also enhanced by relativistic corrections); the string term gives a strictly positive contribution (which is, however, suppressed by relativistic corrections).

The lQCD data for the pressure can be well reproduced, see middle panel of Fig. 5. It is interesting to decompose the pressure into contributions from quasiparticles ($\Omega_{\rm qp} \propto \ln(-G^{-1}) + \Sigma G$) [57] and the two-body interaction characterized by the resummed LWF [$\Phi \propto 1/2 \log(1 - VGG)$]. The latter turns out to be generally small, no more than 15% of the total and slightly increasing with the temperature, cf. right panel of Fig. 5. This suggests that there are no marked changes in the interaction strength or degrees of freedom in the WCS for the QGP in the considered temperature range.

4. Spectral structure of QGP

Finally, let us inspect the spectral structure of the QGP within the WCS. The spectral properties of single partons are summarized in Fig. 6 in terms of their self-energies (real and imaginary parts) and spectral functions. The widths (or scattering rates) of the partons, $\Gamma = -2{\rm Im}\Sigma$, are significantly smaller than their masses, implying that they remain well-defined quasiparticles at all momenta and over the full temperature range. At the lowest temperature, $T = 194$ MeV, the light-parton width is around 0.11 GeV, which is larger than the perturbative expectation, $\frac{4}{3}\alpha_s T \approx 0.07$ GeV, but lower than, e.g., the most recent dynamical quasiparticle model results [71], which are around 0.2 GeV. Similar to the static case, the width rises slightly stronger than linear with temperature, which is closer to the perturbative than the dynamical quasiparticle approach. The 3-momentum dependence of the width is quite strong at low temperature and quite weak at high temperature. This is probably so because partons at different thermal momenta will probe different regimes of the potential, in particular since at high temperature the string term (which is responsible for an appreciable long-range force) is heavily screened. In the infrared region, the confining interaction behaves as $1/m_s^4$ while the Coulomb one as $1/m_d^2$. Thus, the increase of m_s implies a larger decrease of the strength of the string relative to the Coulomb force (the latter is also augmented by the relativistic Breit correction that reduces the momentum dependence). The width of the different quark species are quite similar whereas the gluon width is almost twice larger due to

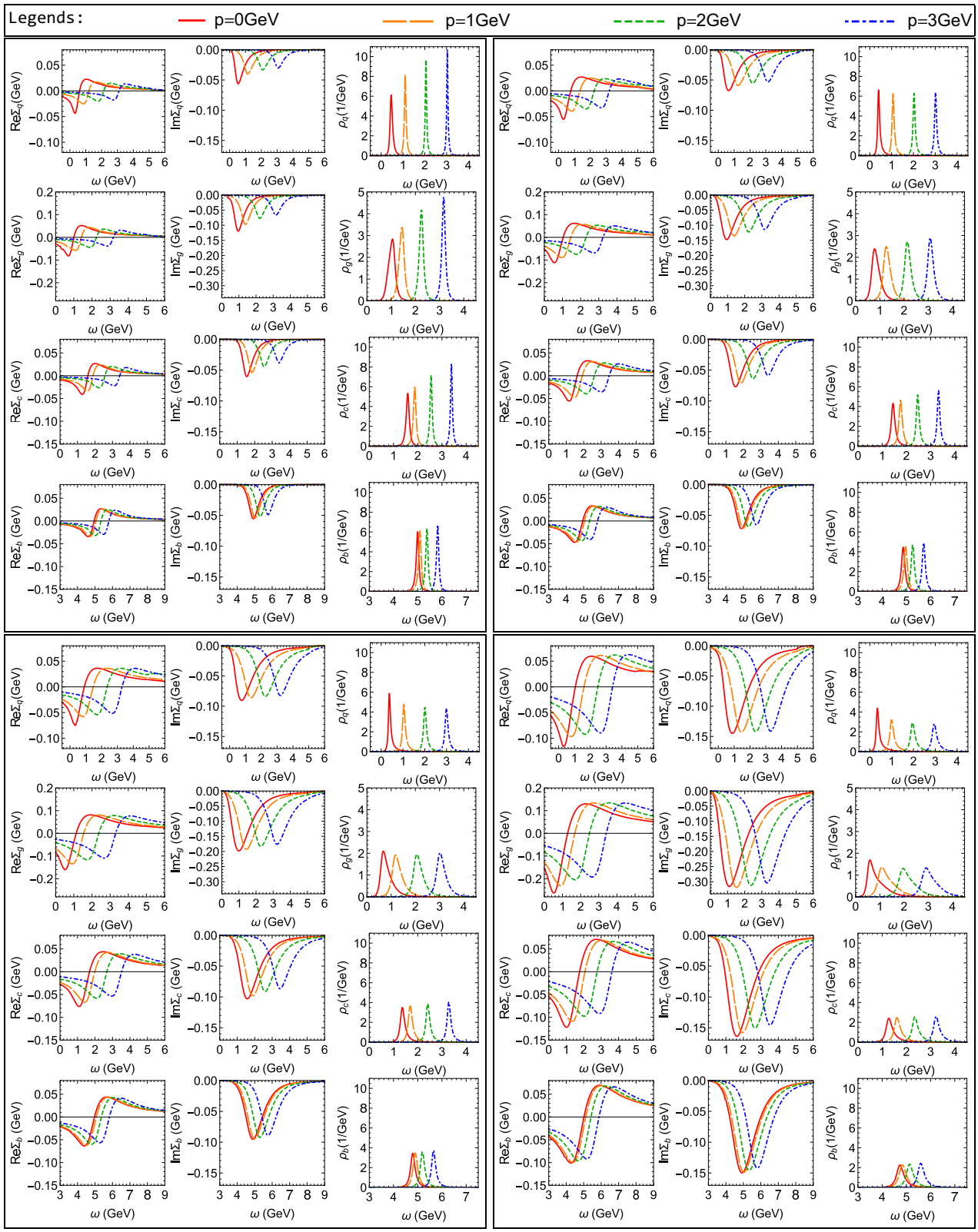

FIG. 6. *Weakly* coupled solution for parton spectral properties of the QGP. The figure is organized into four 3-by-4 panels of 12 plots, with each panel for a given temperature (upper left: $T = 0.194$ GeV, upper right: $T = 0.258$ GeV, lower left: $T = 0.320$ GeV and lower right: $T = 0.400$ GeV). Each panel contains four rows corresponding to different parton species (light quarks (q), gluons (g), charm quarks (c), and bottom quarks (b) in the first, second, third, and fourth row of each panel, respectively). Each row contains three panels showing (from left to right) the energy dependence of the pertinent real and imaginary part of the self-energy and the resulting spectral functions, for four different values of the single-parton 3-momentum (p) in the thermal frame.

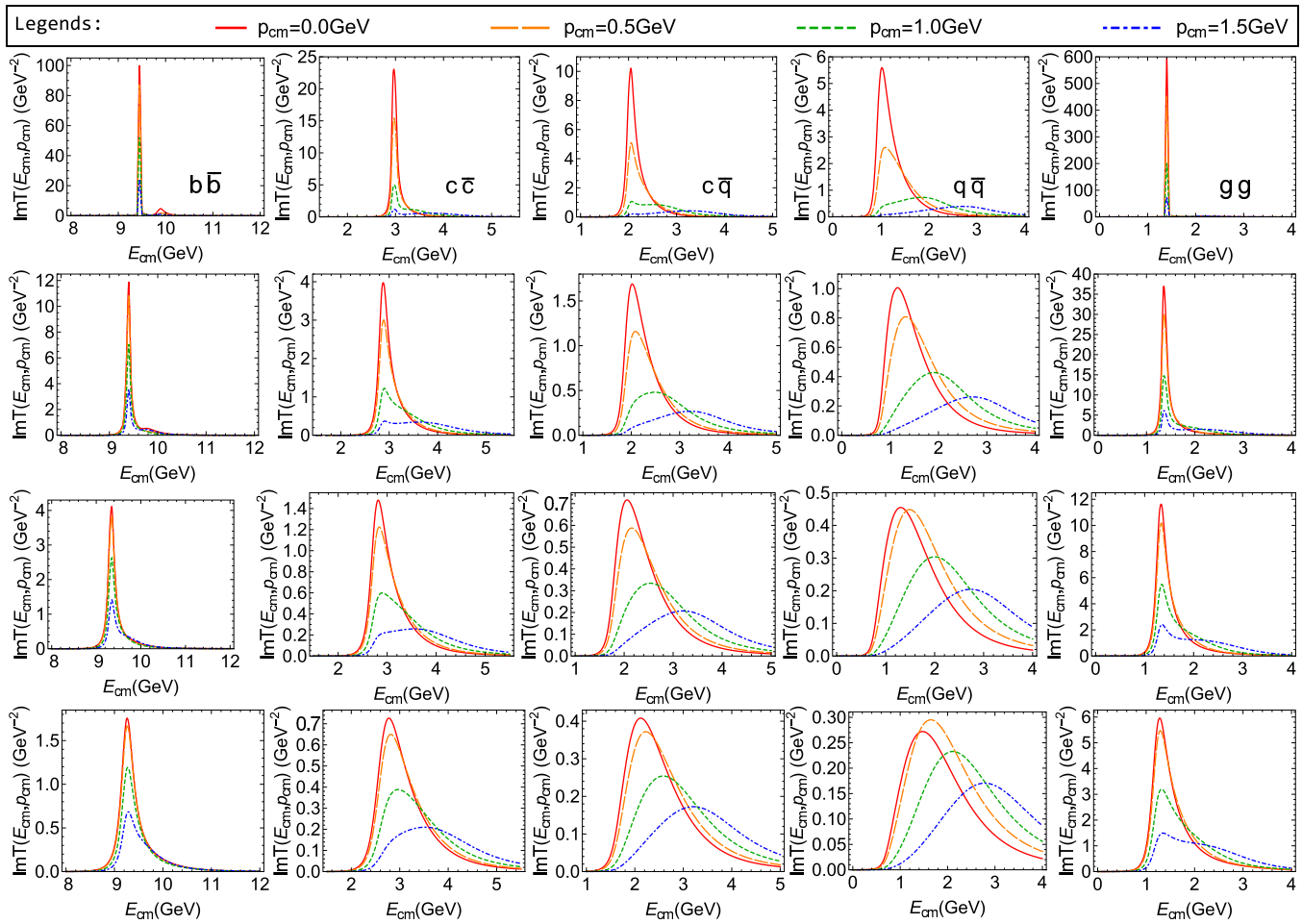

FIG. 7. *Weakly* coupled solution for the imaginary part of the color-singlet S-wave T-matrices (without interference effects) in the bottomonium ($b\bar{b}$; first column), charmonium ($c\bar{c}$; second column), D-meson ($c\bar{q}$; third column), light-quark ($q\bar{q}$; fourth column), and glueball (gg, last column) channels. The four rows correspond to different temperatures, $T = 0.194$ GeV, $T = 0.258$ GeV, $T = 0.320$ GeV, and $T = 0.400$ GeV from top down; in each panel, the T-matrix is displayed for four different values of the single-parton 3-momentum ($p_{\rm cm}$) in the two-body CM frame.

the color Casimir factor. The quark width first increases with mass and then decreases again. Usually a larger mass has a stronger scattering amplitude in the CM frame (cf. Fig. 7), but the CM transformation, Eq. (11), effectively shrinks the phase space. This competition leads to the nonmonotonic behavior.

The underlying two-body correlations are illustrated by the (imaginary part of the) pertinent T-matrices, used to calculate the single-parton self-energy, in Fig. 7. They exhibit a sequential dissociation according to the reduced mass of the bound state. If we use a vanishing binding energy (relative to the constituent two-body mass threshold) to distinguish bound and scattering states (for total momentum $P = 0$), light mesons are melted at $T = 0.194$ GeV while the heavy-light meson, glueball, and quarkonium still survive. The D-meson and first-excited bottomonium state (Υ_{2S}) melt near $T = 0.258$ GeV, the charmonium around $T = 0.320$ GeV and the ground-state bottomonium Υ_{1S} above $T = 0.400$ GeV. Even after melting, a resonance structure can still survive to somewhat higher temperatures, albeit with typically much reduced strength in the T matrix. As an alternative way to characterize the resonance correlation one can inspect their robustness with increasing single-parton CM momentum (essentially going off-shell), the light, heavy-light, and first-excited bottomonium states disintegrate for $p_{\rm cm} \gtrsim 1$ GeV. We finally note that the $q\bar{q}$ bound-state mass at the lowest temperature, $M_{q\bar{q}} \simeq 1$ GeV, is significantly larger than the vacuum mass of the light vector mesons, $m_{\rho,\omega} \simeq 780$ MeV (we recall that we do not include spin-spin or topologically induced interactions, e.g., instanton-induced ones, which are believed to play a key role for dynamical chiral symmetry breaking and its associated Goldstone bosons).

B. Strongly coupled solution

In this section we discuss our self-consistent set of results for a strongly coupled solution (SCS). The section structure parallels the one of the WCS, namely starting from the determination of the underlying potential through fits of lQCD results for the static $Q\bar{Q}$ free energy (Sec. IV B 1), followed by the quarkonium correlator analysis (Sec. IV B 2), the fit to the QGP EoS (Sec. IV B 3) and a discussion of the one- and two-body spectral properties (Sec. IV B 4).

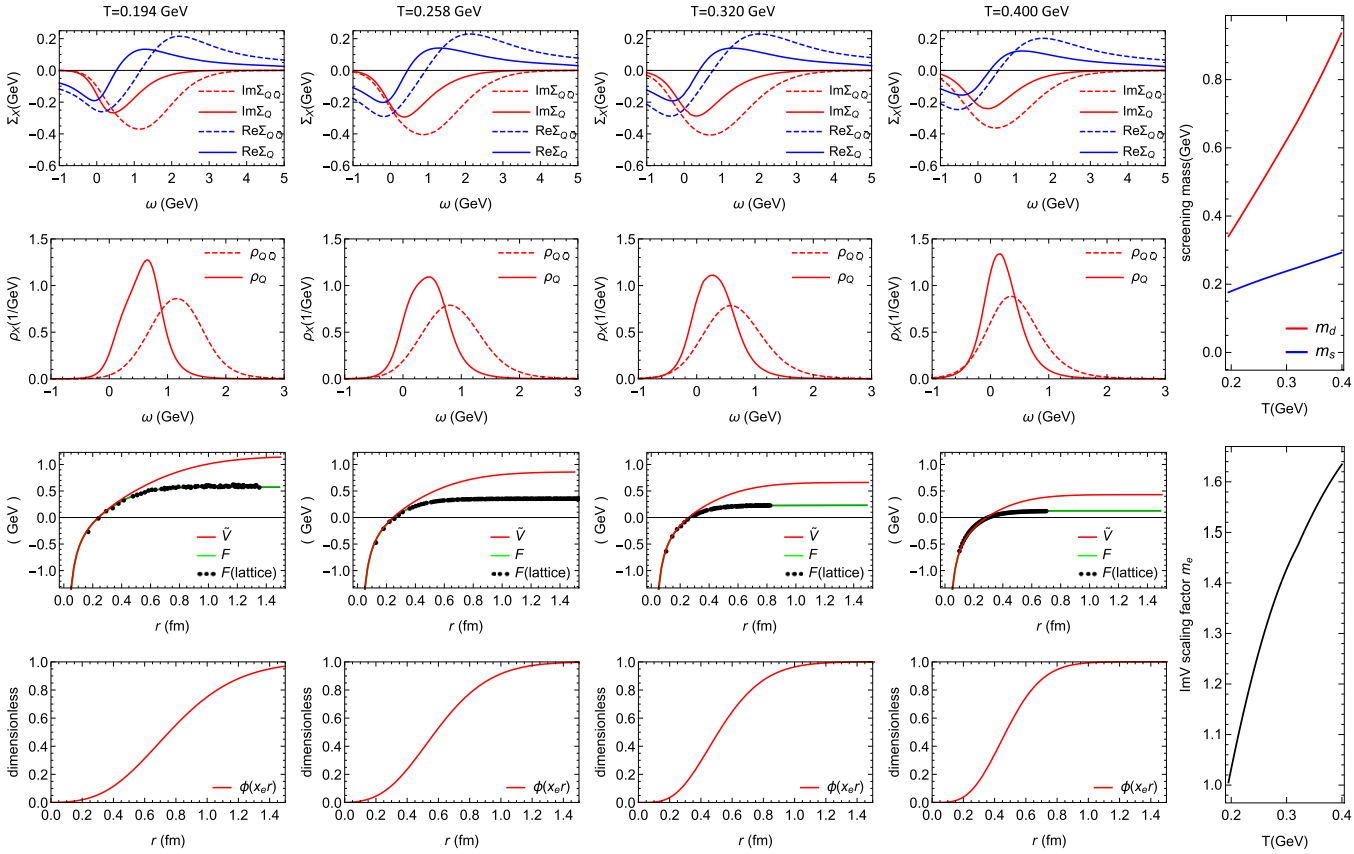

FIG. 8. Results of a *strongly* coupled solution for the self-consistent fit to extract the static HQ potential: single-quark and $Q\bar{Q}$ self-energies, $\Sigma_X(\omega,\infty)$ (first row), and spectral functions, $\rho_X(z,\infty)$ (second row), potential $\tilde{V}(r)$ and free energies (third row), and interference function, $\phi(x_e r)$ (fourth row), in the first four columns corresponding to different temperatures. The last column shows the temperature dependence of the fitted screening masses (top panel) and the scale factor, x_e (bottom panel), figuring in the interference function. The free-energy lQCD data are from Ref. [48].

1. Free energy, potential, and static self-energies

When searching for a SCS within our framework, we start from a trial potential significantly larger than the free energy, together with large imaginary parts in the static-quark self-energies. The converged self-consistent parameters take the values $\alpha_s = 0.27$, $\sigma = 0.225$ GeV^2, $c_b = 1.3$, and $c_s = 0.01$. The strong coupling constant and the "string-breaking" coefficient, c_b, are essentially the same as for the WCS, and the string tension is only about ∼5% larger. The key difference lies in the coefficient, c_s, for the screening mass of the string term, which is a factor of ∼10 smaller. Consequently, the temperature-dependent screening mass, $m_s = (c_s m_d^2 \sigma/\alpha_s)^{1/4}$, turn out to be smaller than in the WCS, mostly at low temperatures, by up to about 1/3, cf. upper right panel Fig. 8. At the same time, the Coulomb Debye mass, m_d, for the SCS is comparable to the one in the WCS at low temperature, but increases more strongly (and essentially linear) with temperature. The key feature of the SCS in-medium potential is thus a rather long-range remnant of the confining force, as shown by the red lines in the third row of Fig. 8. In particular, at intermediate and large distances, the potential rises markedly over the free energy (green lines), by up to 0.6 GeV at the lowest temperature ($T = 0.194$ GeV) and by up to 0.3 GeV at $T = 0.400$ GeV. The latter is not far anymore from the WCS. The fit to the lQCD data (black dots) is of the same quality as for the WCS. The scale factor of the interference function (shown in the lower right panel of Fig. 8) is also very similar to the WCS, although its magnitude is smaller at higher temperatures.

With the extracted potential, the self-energies and spectral functions of the static quark generated from the static-light T-matrices are shown in the first two rows of Fig. 8. At low $T = 0.194$ GeV, the peak value of $\mathrm{Im}\Sigma_Q \approx -0.26$ GeV implies a width of the spectral function in excess of 0.5 GeV. In fact, the full-width at half-maximum of the pertinent spectral function amounts to about 0.7 GeV, due to additional effects from the real part of the static-quark self-energy. This is almost an order of magnitude larger than the leading-order HTL result [59,60,64], $(\frac{4}{3}\alpha_s T) \approx 0.07$ GeV. In addition, the peak value of the single-quark width, $-2\mathrm{Im}\Sigma_Q$, increases only slightly with T at lower temperatures, and even decreases between 0.320 and 0.400 GeV. This remarkable feature is due to the marked loss of long-range interaction strength which can over-compensate the increase in parton density with temperature. For the two-body quantities, the peak value of $\mathrm{Im}\Sigma_{Q\bar{Q}}$ defined in Eqs. (47) and (53) is less than twice the peak value of $\mathrm{Im}\Sigma_Q$, and the width of the two-body spectral function is less than twice that of the single static-quark spectral function. This is different from the WCS case and caused by large off-shell effects.

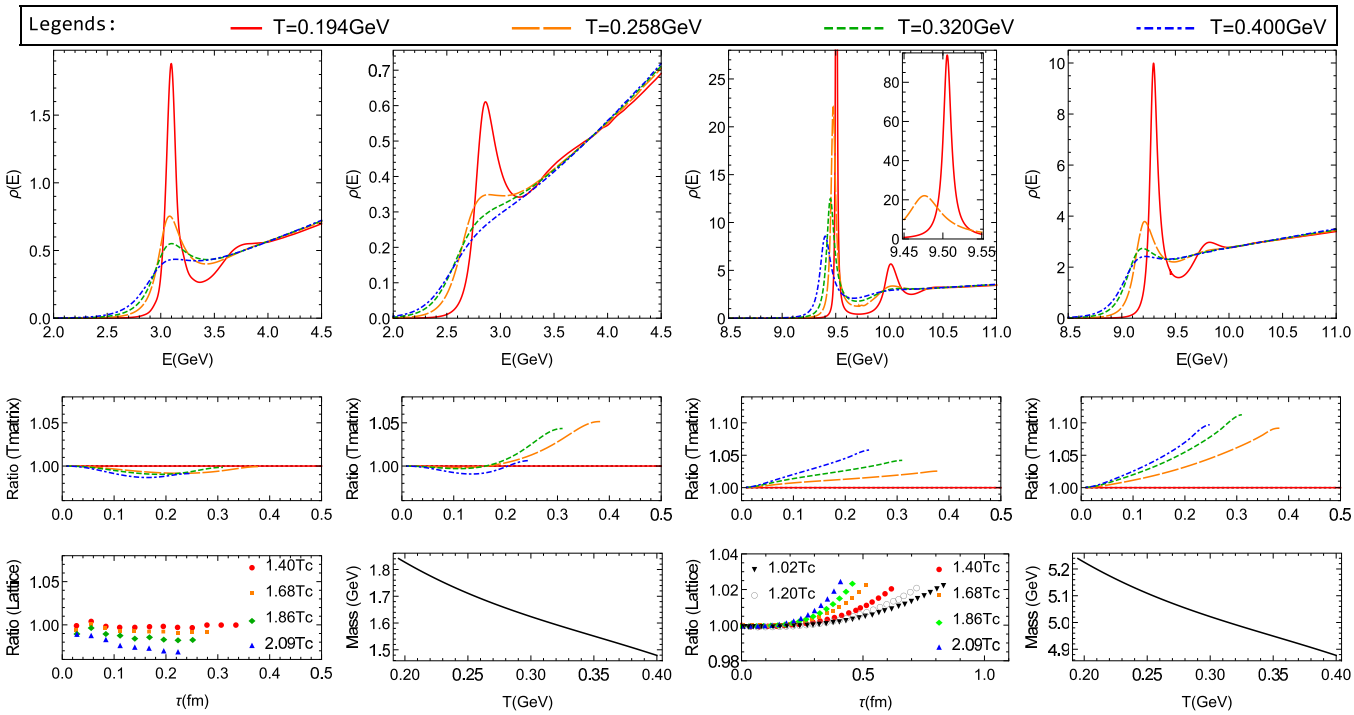

FIG. 9. *Strongly* coupled solution for charmonium (η_c, left panels) and bottomonium (η_b, right panels) spectral functions (upper panels) and correlators ratios (middle panels) with (first and third column) and without (second and fourth column) interference effects in the imaginary part of the potential. The lQCD data for η_c [51] and η_b [52] correlator ratios are shown in the first and third bottom panel, respectively, while the second and fourth bottom panel display the temperature dependence of the charm- and bottom-quark mass, respectively.

Let us also comment on a comparison of the SCS to our previous work in Ref. [17]. The general shape and temperature behavior of the SCS potential are quite similar to the result with our previous fit ansatz [17]. However, the SCS potential shown in Fig. 8 has a significantly smaller force at large distances compared to the earlier result. Due to the increasing shell volume, $\propto r^2$, a long-range force interacts with increasingly more medium particles, which in principle can generate (very) large scattering widths. However, the self-consistency requirement ties the width to the potential as the latter generates the self-energies through the T-matrix. Large widths generated by long-distance forces can therefore easily lead to free energies which fall below the lQCD data. In this way, the self-consistency much augments the control over the properties of the force which are especially effective in generating large widths (in particular its large-distance behavior).

We cannot prove that our SCS constitutes an upper limit for the coupling strength of the QGP, given the lQCD data that we incorporate in our fit. However, there are several limiting factors (in addition to the one described above) which prevent us from constructing more strongly coupled solutions. In particular, we limited ourselves to scenarios where the string tension does not significantly exceed the vacuum value. We also refrained from using "unnaturally" small Coulomb Debye masses which could provide a long-range force but would be in conflict with the expected approach toward perturbative behavior at high temperatures. Within these constraints the presented SCS is the "strongest" solution we could find upon varying our input and ansatz for the initial potential. As one would expect from a self-consistent quantum framework, we have evidence that our calculations respect lower quantum bounds for transport coefficients, as has been conjectured, e.g., for the ratio of shear viscosity to entropy density. For example, if we attempt to push for an extremely long-range force ansatz (which, as explained above, leads to very large scattering widths), the self-consistent iteration procedure in fitting the free energy will push back toward a more weakly coupled solution. When neglecting the requirements to agree with lQCD data and deliberately increasing the interaction strength in the calculation of the EoS, the self-consistent T-matrix iteration ultimately leads to a zero-mass color-singlet glueball, which signals condensation and at that point goes beyond our current setup (recall that our parton fit masses encode possible condensate gaps). Quantum self-consistency clearly plays a key role as a limiting mechanism.

2. *Quarkonium correlators and spectral function*

The self-consistent charmonium and bottomonium spectral functions and pertinent Euclidean correlators ratios (normalized to the lowest-temperature one) are collected in Fig. 9 together with lQCD data for the latter and the temperature dependence of the effective charm- and bottom-quark masses.

The large scattering rates of charm and bottom quarks in the SCS induce significantly larger widths of the quarkonium states than in the WCS. As before, interference effects lead to a marked reduction of the bound-state widths. The stronger binding compared to the WCS is counteracted by the significantly larger heavy-quark masses in medium as to generate

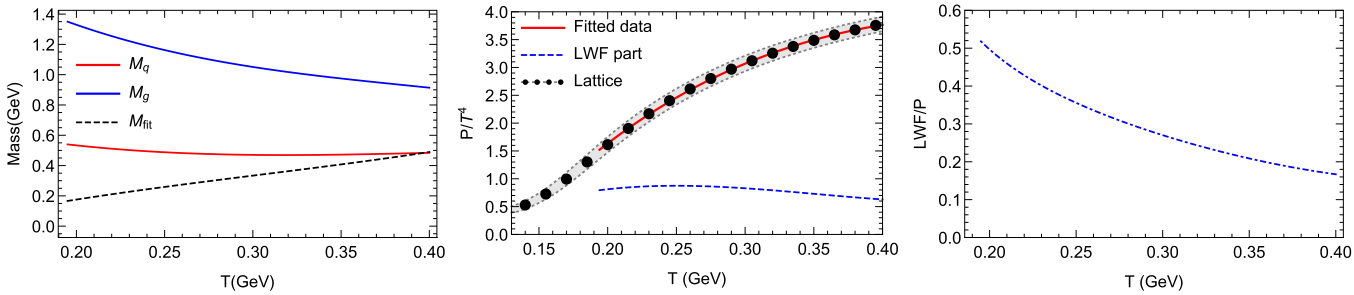

FIG. 10. *Strongly* coupled solution for the QGP bulk medium: fit results of the input masses for quarks and gluons (left panel), the QGP pressure in comparison to lQCD data [46] (middle panel: solid line, total; dashed line, LWF contribution), and the ratio of LWF contribution to total pressure (right panel).

an η_c mass that is remarkably stable with temperature. This leads to Euclidean correlator ratios which are within 2% of unity, which agrees even better with the lQCD data than in the WCS (although this is not necessarily significant, as we argued in the context of the WCS results). The correlator ratios without interference effects deviate somewhat more from the lQCD data, possibly indicating that a moderately broadened charmonium ground state that survives to higher temperatures (here about $T = 0.320$ GeV when including interference) may be favored by lQCD data.[8] For example, the inelastic width of the η_c at T=0.194 GeV is around 0.1 GeV for the SCS and 0.02 GeV for the WCS (including interference). Appreciable charmonium reaction rates with the ground state surviving over an extended interval in temperature are favored by the phenomenology of transport models in describing J/ψ production at RHIC and the LHC [72], in particular to regenerate a sufficient number of J/ψ's at the LHC.

In the Υ sector, the first excited state still survives at the lowest temperature; even without interference effects, a pertinent maximum structure in the spectral function is visible below the nominal $b\bar{b}$ threshold of $2m_b$, but its width is comparable or even larger than the binding energy so that it appears as being dissolved. The ground-state $\Upsilon(1S)$ clearly survives up to the highest temperature, $T = 0.400$ GeV (it is smeared out at much lower temperature without interference effects). The pertinent correlator ratio is in line with lQCD data within a few percent, which again is the closest agreement between all four scenarios considered in this paper (SCS and WCS with and without interference effects). The slight increase of the calculated ratio is in part caused by the lowering of the bound-state mass, implying that the decrease in the constituent bottom-quark masses is more relevant than the decrease in binding energy.

[8]There is a small overall shift of the ground states' peak position to higher masses when including interference effects as compared to neglecting them; this may depend on our specific implementation of the interference effects which requires further investigation. On the other hand, the reduction of the width by interference is a robust mechanism independent of the implementation.

3. QGP equation of state

Next, we turn to the SCS for QGP bulk properties. The fitted light-parton masses are qualitatively similar to the WCS, cf. left panel of Fig. 10. Most notably, the gluon mass is quite a bit larger due to the larger string-induced Fock term contribution, recall Eq. (76), implying a much increased infinite-distance limit relative to the WCS. This contribution is also active for the effective quark mass. The underlying fit mass, $M_{\rm fit}$, is actually appreciably smaller than in the WCS, with values of 0.16 and 0.49 GeV at $T = 0.194$ GeV and $T = 0.400$ GeV, respectively. These values are not far from what one expects from the perturbative (Coulomb) thermal masses, $\sqrt{1/3}gT = 0.2$ GeV and $\sqrt{1/3}gT = 0.42$ GeV, respectively. The resulting EoS fits lQCD data well, and encodes the most important difference between SCS and WCS, namely that the two-body contribution to the pressure is much more prominent at low temperatures, reaching more than 50% at $T = 0.194$ GeV, compared to ∼10% in the WCS. Also, the LWF contribution shows a more intuitive temperature behavior, in that its fraction relative to the total appreciably decreases with increasing T (cf. right panel of Fig. 10); here, the decrease in interaction strength surpasses the increase in parton density, which can be interpreted as a gradual melting of the light-parton bound states with T (this interpretation will become even clearer upon inspection of the spectral functions in the next section). However, at $T = 0.400$ GeV, the interaction contribution still amounts to ∼20%, indicating that even at this temperature the QGP contains a significant nonperturbative component (possibly driven by the gluonic sector through glueball contributions). As before, the gluon sector largely decouples at small temperatures due to the large gluon masses.

4. Spectral structure of QGP

We finally turn to the examination of the single-parton spectral functions and their in-medium scattering amplitudes. The width of the partons, $\Gamma = -2\mathrm{Im}\Sigma$, is large, especially at low temperatures and small 3-momenta, $p \lesssim T$, see the upper four plots in the second column of Fig. 11. The quark (gluon) width reaches up to 0.6 (1.1) GeV right around its on-shell energy, which is larger than its effective mass and thus implies the loss of a well-defined quasiparticle excitation. Inspection of the pertinent $p = 0$ light-parton spectral functions (upper 2 panels in the third column of Fig. 11) confirms this notion, as

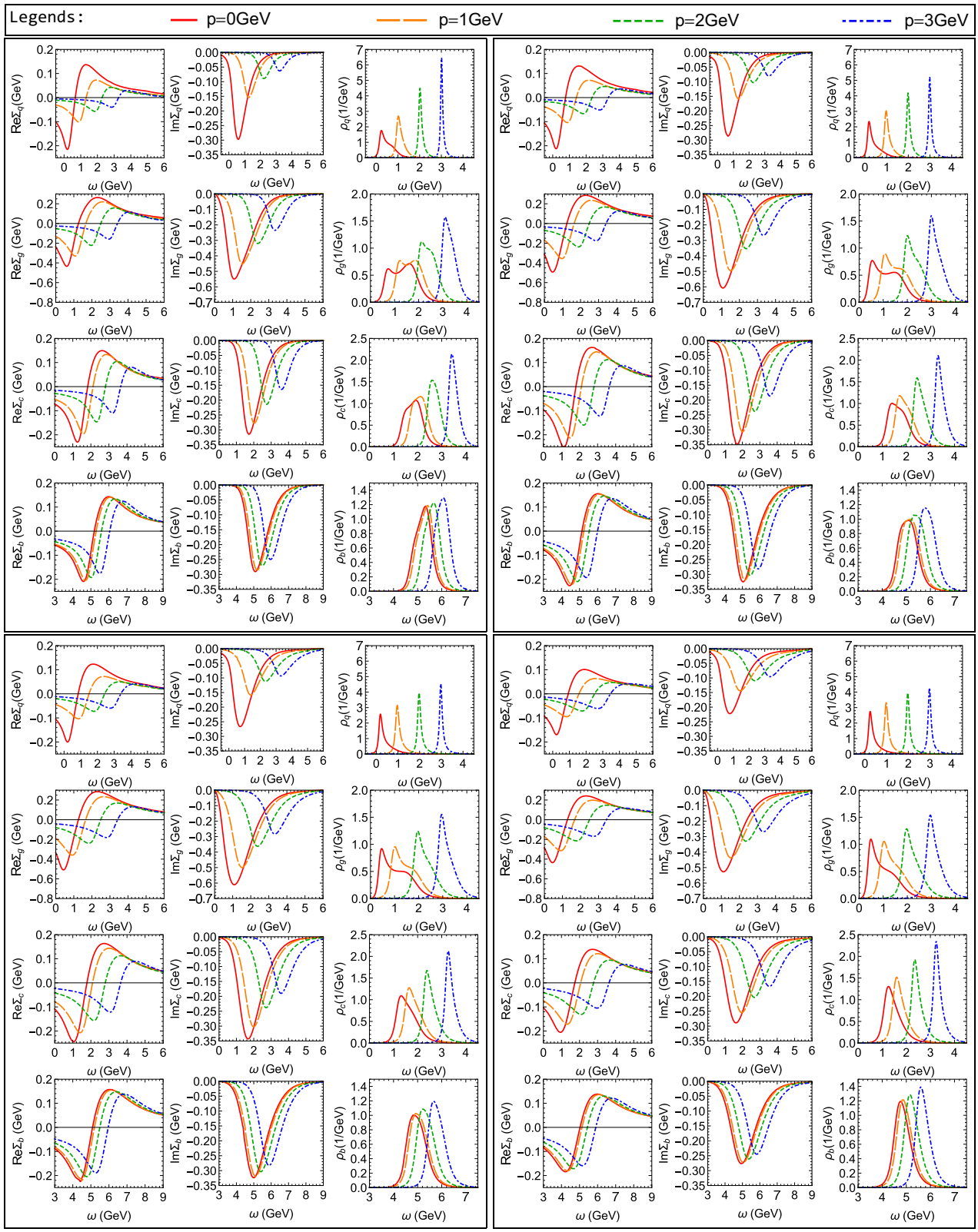

FIG. 11. *Strongly* coupled solution for parton spectral properties of the QGP. The figure is organized into four 3-by-4 panels of 12 plots, with each panel for a fixed temperature (upper left: $T = 0.194$ GeV, upper right: $T = 0.258$ GeV, lower left: $T = 0.320$ GeV and lower right: $T = 0.400$ GeV). Each panel contains four rows corresponding to different parton species (light quarks (q), gluons (g), charm quarks (c), and bottom quarks (b) in the first, second, third, and fourth row of each panel, respectively). Each row contains three panels showing (from left to right) the energy dependence of the pertinent real and imaginary part of the self-energy and the resulting spectral functions, for four different values of the single-parton 3-momentum (p) in the thermal frame.

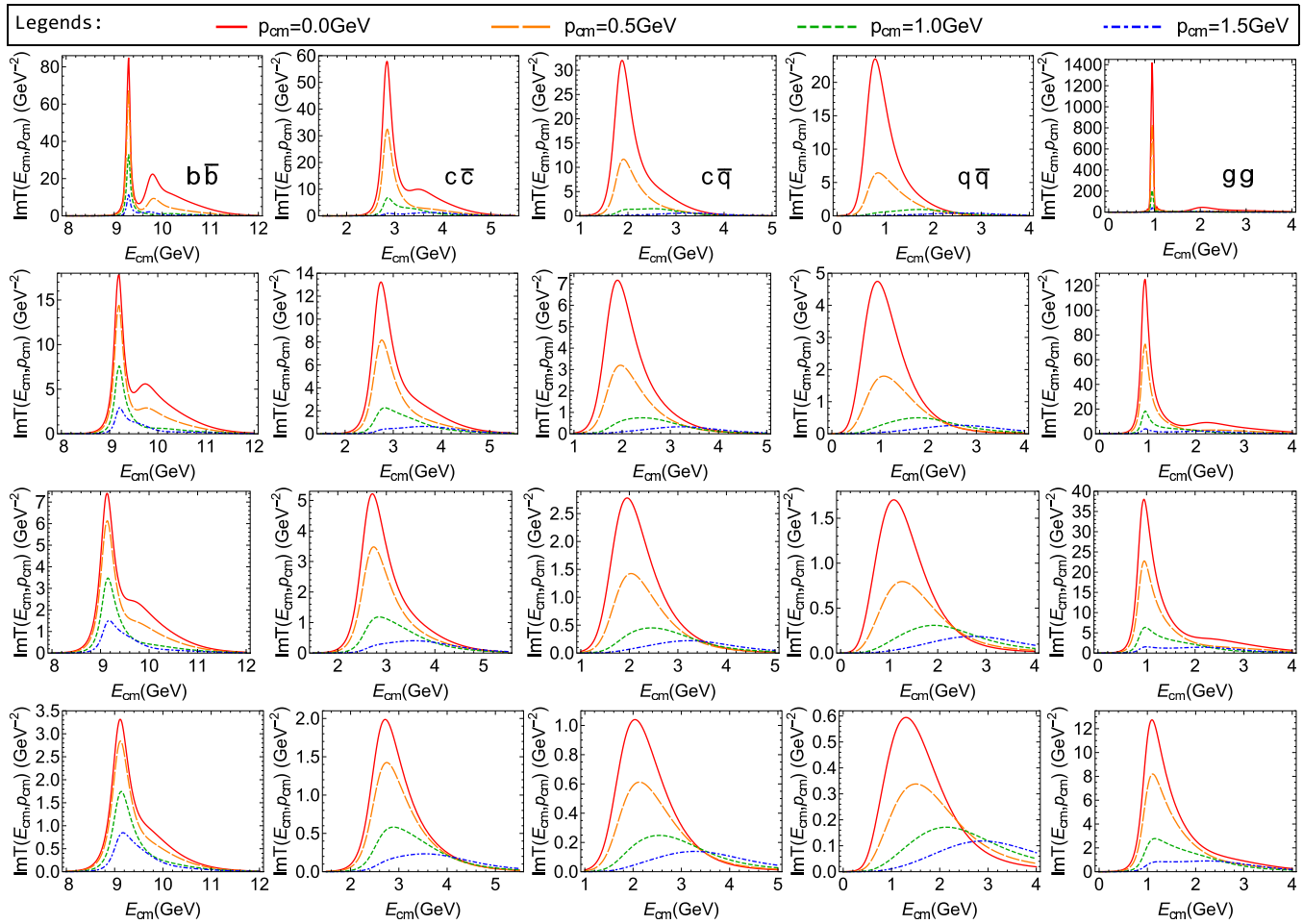

FIG. 12. *Strongly* coupled solution for the imaginary part of the color-singlet S-wave T-matrices (without interference effects) in the bottomonium ($b\bar{b}$; first column), charmonium ($c\bar{c}$; second column), D-meson ($c\bar{q}$; third column), light-quark ($q\bar{q}$; fourth column), and glueball (gg, last column) channels. The four rows correspond to different temperatures, $T = 0.194$ GeV, $T = 0.258$ GeV, $T = 0.320$ GeV, and $T = 0.400$ GeV from top down; in each panel, the T-matrix is displayed for four different single-parton momenta ($p_{\rm cm}$) in the two-body CM frame.

the quark's (gluon's) spectral strength is spread over an energy range of about 1(2) GeV. In fact, the rather large and attractive real part of the self-energy at small (off-shell) energies (upper 2 panels of the first column of Fig. 11) also plays an important part in the quark (gluon) spectral distribution, as it generates a rather prominent collective mode at $\omega \simeq 0.15(0.7)$ GeV, sitting on top of the broad distribution associated with the dissolved quasiparticle mode. The low-temperature widths are almost an order of magnitude larger than the HTL value of $\frac{4}{3}\alpha_s T \approx 0.07$ GeV, and much larger than the most recent dynamical quasiparticle model result which is around 0.2 GeV [71]. Interestingly, the temperature dependence of the parton widths is nonmonotonic with increasing temperature (as was found for static quarks discussed in Sec. IV B 1), which has important consequences for the temperature dependence of transport coefficients [25]. This is qualitatively different from both perturbative and dynamical quasiparticle approaches. The 3-momentum dependence of the width is quite strong especially at low temperatures (less so at high temperature), being substantially reduced with increasing p. This implies that at higher momenta well-defined quasiparticle excitations re-emerge at any temperature, as to be expected from a generic transition to a weak coupling. However, since the string term at high temperature is not screened as much as in the WCS, the momentum dependence of self-energy at high temperature differs from the WCS. The widths of the charm and bottom quarks are quite similar to the light quarks, implying that bottom quarks remain well-defined quasiparticles at all momenta and temperatures, while the situation is borderline for low-momentum charm quarks close to T_c.

Self-consistent T-matrices are compiled in Fig. 12. At low temperatures appreciably bound quark-antiquark states emerge in all channels (glueballs, light mesons, heavy-light mesons, charmonia, and bottomonia). The light $q\bar{q}$ resonance mass is close to the vacuum mass of light vector mesons, reflecting a realistic vacuum limit as encoded in the potential model (instanton effects are subleading in the vector channel). This is, however, nontrivial given its embedding in the QGP EoS (in particular through the fitted light-quark mass). Note that the off-shell behavior of the parton widths, i.e., their decrease

away from the on-shell peak (recall column two in Fig. 11), plays an important role in the formation of bound states; e.g., the light-meson width of ∼0.6 GeV at the lowest temperature is well below twice the light-quark width, mostly because of the ∼0.3 GeV binding relative to the nominal $q\bar{q}$ threshold of 1.1 GeV. Compared to the WCS (recall Fig. 7), the strength of the T-matrices in the SCS is much increased (e.g., the peak value in the $p_{\rm cm}$=0 light-meson channel is ∼25/GeV^2 in the latter compared to ∼6 /GeV^2 in the former; also, the mass of the $q\bar{q}$ bound state is smaller, ∼0.8 GeV versus ∼1 GeV). This, in particular, makes a large difference in their contributions to the EoS (recall Fig. 10 versus Fig. 5). At the same time, the much larger widths in the spectral functions of light partons in the SCS relative to the WCS causes their thermodynamic weight to be much suppressed in the former relative to the latter. In this sense, the SCS predicts a transition from broad parton quasiparticles to broad hadronic states in the thermodynamics of the QGP as T_c is approached from above. The reemergence of parton quasiparticles and suppression of their bound states not only occurs with increasing temperature (note the reduction in the y-axis scale when going down in temperature row by row in Fig. 12), but also with increasing parton CM momentum within the bound state (not to be confused with the total momentum, P, of the bound state in the heat bath, which is zero throughout this paper) and delayed with increasing constituent parton mass.

V. SUMMARY AND OUTLOOK

We have set up a self-consistent thermodynamic T-matrix approach to study the bulk and microscopic properties of the QGP in a unified framework, encompassing both light- and heavy-flavor degrees of freedom. Starting from the HQ limit of QCD, we set up an effective partonic Hamiltonian with a universal color force, including remnants of the confining force and relativistic corrections necessary to treat thermal partons. We have computed one- and two-body thermodynamic Green's and spectral functions self-consistently, incorporating bound and scattering states on an equal footing. Compared to earlier works, a full off-shell treatment is implemented to account for quantum many-body effects rigorously, in particular the collisional widths of the QGP constituents. Moreover, our approach enables systematic constraints on the inputs to the Hamiltonian, i.e., the two-body potential and two effective light-parton mass parameters, by comparing to a variety of lattice-QCD data.

Our calculation of the equation of state has been carried out in the LWB formalism with self-consistently computed light-parton self-energies and T-matrices. Importantly, we managed to resum the Luttinger-Ward functional using a matrix-log technique, which is critical to account for the dynamical formation of bound (or resonance) states in the thermodynamics of the system. The main constraints on the two-body driving kernel are derived from the HQ free energy, $F_{Q\bar{Q}}$, which we have also computed self-consistently from the T-matrix for static quarks embedded in the QGP. Based on a parametric ansatz for an in-medium Cornell potential, we have fitted lattice-QCD data for $F_{Q\bar{Q}}$ and further checked our results against Euclidean correlator ratios in the bottomonium and charmonium sectors. Together with the EoS, for which the fit of pertinent lQCD data can be largely controlled through the two bare light-parton masses in the Hamiltonian, this constitutes a comprehensive quantum many-body framework for light and heavy partons and their two-body correlations in the QGP. We have solved this problem through a multilayered numerical iteration procedure in our fit to the three sets of lQCD data, where a typical accuracy at a few-percent level can be achieved. The main predictive power of the approach resides in the emerging spectral and transport properties of the QGP, including the prevalent degrees of freedom in the EoS.

In our search for self-consistent solutions, it turns out that the above set of lQCD constraints does not uniquely specify the input for the driving kernel. We classified its possible range by a weakly and a strongly coupled solution. In the former, the input potential comes close to a lower limit set by the HQ free energy itself (not unlike what has been discussed based on direct Bayesian extraction methods [16]). The resulting light-parton spectral functions have rather moderate widths, well below their masses, and thus yield well-defined quasiparticles, as well as rather sharp but loosely bound resonances when approaching T_c from above. The latter remain subleading, at a 10% level, in their contribution to the EoS. In contrast, the strongly coupled solution is characterized by a potential that appreciably exceeds the free energy (not unlike recent lQCD extractions reported in Ref. [73]), recall the third row of Fig. 8. The key difference to the weakly coupled solution is a long-range remnant of the confining force (while its short-distance, $r \lesssim 0.4$ fm, and high-temperature, $T > 2T_c$, behavior is quite similar in both solutions). The emerging partonic spectral widths are much enhanced; they become comparable to the parton masses and thus dissolve quasiparticle structures for low-momentum modes near T_c (cf. the third panel in rows 1 and 2 of Fig. 11). At the same time, broad but well-defined two-particle bound states (mesons) emerge (last two panels in row 1 of Fig. 12) and become the leading contribution to the EoS (middle panel in Fig. 10), thus signaling a transition in the degrees of freedom in the system. At high momenta, parton quasiparticles reemerge and bound-state correlations are much suppressed. This solution, in particular, critically hinges on a proper treatment of the quantum effects induced by the large scattering rates.

While we believe that the strongly coupled solution is clearly the more attractive one (including its transition from quarks to hadrons and a qualitatively liquid-like behavior with interaction energies comparable to the parton masses), a more quantitative characterization of this notion is in order. We already indicated in our previous letter [25] that transport coefficients, in connection with heavy-ion phenomenology, can play a decisive role in this regard. The heavy-quark diffusion coefficient and the viscosity-to-entropy density ratio show promisingly small values in the strongly-coupled scenario, while they are significantly larger in the weakly coupled scenario, to an extent that creates conflicts with hydrodynamic and heavy-flavor transport modeling of heavy-ion collisions. The latter is currently being investigated quantitatively and will be reported elsewhere [74]. In fact, converting the heavy-quark diffusion coefficient into a thermalization and scattering rate, one can straightforwardly deduce that values of $2\pi\mathcal{D}_s \simeq 3$

translate into quark scattering rates of order 1 GeV; this implies the dissolution of light quasiparticles, fully consistent with our numerical findings. The large widths also require the underlying potential V to markedly exceed the free energy, $F_{Q\bar{Q}}$, independent of model details [17]. As a compact upshot, the strongly coupled solution found in our approach may be characterized as establishing links between: "a large string potential" $\Leftrightarrow$ "strong two-body resonances" $\Leftrightarrow$ "broad (non-quasiparticle) spectral functions" $\Leftrightarrow$ "small viscosity/spatial diffusion coefficients." If the string term arises from the nontrivial vacuum structure of QCD, then these links suggest that the latter is in fact responsible for the remarkable features of the sQGP.

A more ambitious line of future work is to test the predicted spectral properties more directly; in the quarkonium sector this presumably requires the formulation of quantum transport approaches for heavy-ion collisions as recently discussed in the literature, which, in turn, can take advantage of heavy-quark diffusion properties computed with the same underlying interaction. The most direct connection remains the dilepton production rate, where again constraints from lQCD data can be straightforwardly utilized. Another area accessible to our approach is the investigation of finite chemical potential in the QCD phase diagram, starting with the calculation of quark susceptibilities. However, the description of phenomena associated with dynamical chiral symmetry breaking, which are expected to become important at temperatures below $T \simeq 0.185$ GeV [75], will require an extension of the current formalism to explicitly include condensation mechanisms. This is more challenging but, we believe, still feasible.

ACKNOWLEDGMENT

This work is supported by the U.S. NSF through Grant No. PHY-1614484.

APPENDIX A: T-MATRIX APPROACH FOR LIGHT PARTONS

In this Appendix we discuss several issues related to the implementation of the potential approximation for light-quark interactions. Historically, the Cornell potential has been a successful tool for quark-based hadron spectroscopy; 3D reductions of the 4D Bethe-Salpeter equation (BSE) are also widely used in effective hadronic approaches to hadronic vacuum physics, including light mesons like π-π interactions. In particular, the Cornell potential incorporates essential non-perturbative aspects of the QCD force, i.e., a confining force. Our approach is a finite-temperature version of this framework, where remnants of the confining force turn out to play a crucial role to render a strongly coupled system. The recovery of the vacuum vector-meson masses at low QGP temperatures in the SCS (where the potential is close to its vacuum form) is a direct manifestation of a "realistic" vacuum limit of the approach in the light-quark sector. As we remarked in the text, interactions believed to be essential for spontaneous chiral symmetry breaking (such as instanton-induced forces) are not included, but we recall that recent lQCD computations have found that the effects of chiral symmetry breaking have essentially vanished once the temperature has reached about 30 MeV above the chiral crossover temperature, $T_{\rm pc}^{\chi} \simeq 0.155$ GeV [75].

There are several further considerations. The reduction of the relativistic 4D Bethe-Salpeter equation (BSE) [26] into 3D scattering equations has been scrutinized, e.g., in Ref. [29]. In particular, within in the Blankenbecler-Sugar (BbS) scheme [27], the BSE can be equivalently separated into two coupled equations, where the kernel of the first (leading) equation is potential-like, while the second (subleading) equation quantifies the off-energy-shell corrections to the potential kernel. The philosophy is to expand ithe BSE around the potential solution using a parametrically small correction, $R_2 V$ [27], rather than to expand around the free-wave solution using the coupling constant and/or velocity (as in NRQCD) as a small parameter. In particular, such an expansion does not rely on a nonrelativistic hierarchy. This series usually exhibits a fast convergence [27,29], suggesting that the leading potential solution is already close to the full solution. In many cases, the higher-order off-shell corrections can be effectively absorbed in an adjustment of the potential. In the present case, the fits of the potential to lQCD data may approximately encode such corrections. Finally, we recall that for $2 \to 2$ on-shell scattering in the CM system the in- and outgoing momenta moduli of the particles are equal; i.e., there is no energy transfer in the collision. We also recall that while the two-body interaction is approximated by an instantaneous force, the many-body quantum approach fully accounts for the dynamics (energy dependence) of the one- and two-particle propagators (and T-matrices) in the system. Additional considerations can be found in Refs. [9,76].

APPENDIX B: GENERALIZED THERMODYNAMIC RELATIONS FOR THE LWB FORMALISM AT FINITE μ_q

The LWB formalism implies several thermodynamic relations for particle, energy, and entropy densities [18,20]. However, these relations will be modified when using an effective Hamiltonian whose "bare" single-particle masses [encoded in the dispersion relation $\varepsilon(p)$], and potential, V, depend on temperature (T) and chemical potential (μ). In this Appendix we illustrate these modifications.

The strategy for the derivation is to start from the usual relations without T or μ dependence in the dispersion relation and potential and then generalize them to the case with T and μ dependencies. For derivatives with respect to (wrt) T or μ any implicit dependence through G will vanish. For ε and V independent of T and μ, one has

$$N = -\frac{\delta\Omega}{\delta\mu} = \pm\frac{-1}{\beta}\sum_n \mathrm{Tr}\{G\}, \tag{B1}$$

since the dependence of μ through $(\delta\Omega/\delta G)(\delta G/\delta\mu)$ will vanish according to Eq. (24), and the only μ dependence figures from $G_{(0)}^{-1} = i\omega_n - (\varepsilon - \mu)$.

For the derivation of the energy density from the grand potential one can adopt a method in time space is given in Ref. [20]. In frequency space, with a separation of the β dependence arising from the loop as in Eq. (20), the entropy

contribution can be derived as

$$TS = \beta\frac{\partial\Omega}{\partial\beta} = -\Omega \mp \frac{-1}{\beta}\sum_n \mathrm{Tr}\left\{(-i\omega_n G) + \frac{1}{2}\Sigma(G)G\right\}. \tag{B2}$$

Still, the implicit dependence on β through G will vanish. The first term comes from the derivative wrt $(-1/\beta)$ in the frequency sum in obtaining Ω and Φ. The second term comes from the derivative wrt $(-1/\beta)$ of ω_n in $G^{-1}_{(0)}$. The third term comes from the $(-1/\beta)^\nu$ dependence of the loop integrals in the self-energy and gives a factor ν that cancels the $1/\nu$ factor in the skeleton expansion. With the entropy contribution, the energy U is

$$U = \Omega + TS + \mu N = \pm\frac{-1}{\beta}\sum_n \mathrm{Tr}\left\{\left[\varepsilon + \frac{1}{2}\Sigma(G)\right]G\right\}, \tag{B3}$$

where $G^{-1} = i\omega_n - (\varepsilon - \mu) - \Sigma$ by use of Eq. (25). We can derive Eq. (B3) from Eqs. (B2) and (B1) using $GG^{-1} = 1$ and $\frac{-1}{\beta}\sum_n e^{i\omega_n\epsilon}1 = 0$ with an ϵ regulation technique [44]. This completes the derivation of the standard thermodynamic relations within the LWB formalism.

If the "bare" single-particle dispersion relation ε and the potential V of the Hamiltonian are functions of β and μ, the particle number, N, and internal energy, U, receive extra contributions,

$$N = \pm\frac{-1}{\beta}\sum_n \mathrm{Tr}\left\{\left[1 - \frac{\partial\varepsilon}{\partial\mu} - \frac{1}{2}\Sigma\left(G,\frac{\partial V}{\partial\mu}\right)\right]G\right\}, \tag{B4}$$

$$U = \pm\frac{-1}{\beta}\sum_n \mathrm{Tr}\left\{\left[\varepsilon + \beta\frac{\partial\varepsilon}{\partial\beta} - \mu\frac{\partial\varepsilon}{\partial\mu} + \frac{1}{2}\Sigma(G) + \frac{1}{2}\Sigma\left(G,\beta\frac{\partial V}{\partial\beta}\right) - \frac{1}{2}\Sigma\left(G,\mu\frac{\partial V}{\partial\mu}\right)\right]G\right\}, \tag{B5}$$

where $\Sigma(G,X) \equiv \sum_\nu \Sigma_\nu(G,X)$, and $\Sigma_\nu(G,X)$ is defined to replace one of the V in evaluating $\Sigma_\nu(G)$ by X at each order. It can be shown that, at least for ladder and ring diagrams, it does not matter which V is replaced in the diagram because every V in the connected diagram for Φ_ν is equivalent. Thus, for the T-matrix resummation the self-energy can be schematically written as

$$\Sigma(G,X) = T(G,X)G,\ T(G,X) = (1 - VGG)^{-1}X, \tag{B6}$$

where X is $\mu\frac{\partial V}{\partial\mu}$ or $\beta\frac{\partial V}{\partial\beta}$. Since $T(G,V) = (1 - VGG)^{-1}V$, the new logarithm can be adapted from the original T-matrix logarithm without increasing the complexity.

APPENDIX C: ADDITIONAL RELATIONS FOR THE STATIC HQ FREE ENERGY

Based on the setup in Sec. III B, we discuss additional useful relations that follow from this formalism.

First, we prove that a relation $F_{Q\bar{Q}}(\infty,\beta) = 2F_Q(\beta)$ is implicit in our formalism for the Polyakov loop defined as

$$F_Q(\beta) = \frac{-1}{\beta}\ln\left[\frac{-1}{\beta}\sum_{\nu_n} G_{\bar{Q}}(i\nu_n)e^{-i\nu_n\beta}\right]. \tag{C1}$$

If we express Eq. (38) in frequency space,

$$F_{Q\bar{Q}}(r,\beta) = \frac{-1}{\beta}\ln\left[\frac{-1}{\beta}\sum_{E_n} G_{Q\bar{Q}}(iE_n,r)e^{-iE_n\beta}\right], \tag{C2}$$

use the fact that $\tilde{G}_{Q\bar{Q}}(iE_n,\infty) = G^0_{Q\bar{Q}}(iE_n) = -\beta^{-1}\sum_{\nu_n} G_Q(iE_n - i\nu_n)G_{\bar{Q}}(i\nu_n)$ and $iE_n = i\omega_n + i\nu_n$ with the identity

$$\frac{-1}{\beta}\sum_{E_n}\frac{-1}{\beta}\sum_{\nu_n} G_Q(iE_n - i\nu_n)G_{\bar{Q}}(i\nu_n)e^{-iE_n\beta} = \left(\frac{-1}{\beta}\sum_{\omega_n} G_Q(i\omega_n)e^{-i\omega_n\beta}\right)\left(\frac{-1}{\beta}\sum_{\omega_n} G_{\bar{Q}}(i\nu_n)e^{-i\nu_n\beta}\right), \tag{C3}$$

and plug this into Eq. (C2), one indeed finds $F_{Q\bar{Q}}(\infty,\beta) = 2F_Q(\beta)$, which is also satisfied numerically.

Second, we found the following identity:

$$\tilde{V}(r) = \int dE[E\rho_{Q\bar{Q}}(E,r)] = \lim_{t\to 0} i\frac{\partial}{\partial t}G^>(t,r), \tag{C4}$$

which can be proved using a contour integral (over the large upper half circle) and the fact that $\Sigma_{Q\bar{Q}}(z,r)$ is analytic (reaching 0 at large z) for

$$\tilde{V}(r) = \frac{-1}{\pi}\mathrm{Im}\left[\int dz\frac{z}{z - \tilde{V}(r) - \Sigma_{Q\bar{Q}}(z,r)}\right]. \tag{C5}$$

We note that $\tilde{V}(r)$ is different from the definition in Ref. [58], where it is for the long-time limit. In our approach, $V(r) = \tilde{V}(r) - 2\Delta M_Q$ is the fundamental potential figuring in the Hamiltonian which will not contain an imaginary part and reach 0 at infinite r.

Third, we propose a possible way to obtain further constraints on the potential from lQCD data for the Wilson line, $G_{Q\bar{Q}}(\tau,r)$ [16,58,77], which in our context is given by

$$G_{Q\bar{Q}}(-i\tau,r) = \int_{-\infty}^{\infty} dE\,\rho_{Q\bar{Q}}(E,r)\,e^{-\tau E}. \tag{C6}$$

These data sets can in principle provide information beyond the free-energy data. Ideally, $\rho_{Q\bar{Q}}(E,r)$ can be obtained by inverting the $e^{-\tau E}$ kernel. This leads to

$$G^0_{Q\bar{Q}}(z) = \int dE\frac{\rho_{Q\bar{Q}}(E,\infty)}{z - E},$$
$$V(z,r) = \left[G^0_{Q\bar{Q}}(z)\right]^{-1} - \left[\int dE\frac{\rho_{Q\bar{Q}}(E,r)}{z - E}\right]^{-1}. \tag{C7}$$

From $V(z,r)$, we can separate the input static potential $V(r)$. However, a direct inversion of the kernel $e^{-\tau E}$ in Eq. (C6) is challenging. In our approach, we can instead calculate the spectral function $\rho_{Q\bar{Q}}$ based on quantum many-body physics

with a potential ansatz just as in the main body of this paper. This extra information may help to narrow down the current latitude between WCS and SCS.

APPENDIX D: INTERFERENCE EFFECTS AND Im V

In this Appendix, we illustrate the origin of r-dependent imaginary part of the potential in terms of interference effects at the three-body level and discuss future directions to define $\Sigma_{Q\bar{Q}}(z,r)$ self-consistently embedded in the T-matrix approach. We illustrate potential conceptual problems for "Im V" and outline how they may be handled within the T-matrix framework.

The interference effects are diagrammatically illustrated in the first row of Fig. 13. A medium parton (top line) can scatter with either of the heavy quarks (lower two lines) interacting with each other. Therefore, the diagram equation can be schematically represented by $(\mathcal{M}_Q+\mathcal{M}_{\bar{Q}})(\mathcal{M}_Q^\dagger+\mathcal{M}_{\bar{Q}}^\dagger)$. In analogy to squaring the usual coherent supposition of two quantum amplitudes, it can be separated into a noninterfering term, $|\mathcal{M}_Q|^2+|\mathcal{M}_{\bar{Q}}^\dagger|^2$, and an interfering term, $\mathcal{M}_Q\mathcal{M}_{\bar{Q}}^\dagger+\mathcal{M}_{\bar{Q}}\mathcal{M}_Q^\dagger$. Moreover, the amplitude squared of the three-body diagram corresponds to the imaginary part of the two-body diagram by cutting the internal loops, which is the optical theorem. Thus, in the second row of Fig. 13 we can identify the first two cuts in the self-energy diagram corresponding to the noninterfering term and the two cuts in the screening diagram corresponding to the interference term. The r-independent "Im V" is the imaginary part of self-energy while the r-dependent "Im V" (proposed by in Ref. [60]) is the interference term.

The originally proposed "Im V" is based on perturbative diagrams. Motivated by the correspondence between the diagrams in the first two rows of Fig. 13, and calculating the self-energies from the T-matrix by the first two diagrams in the third row of Fig. 13, the interference term should correspond to the third diagram in the third row. The T-matrix configuration,

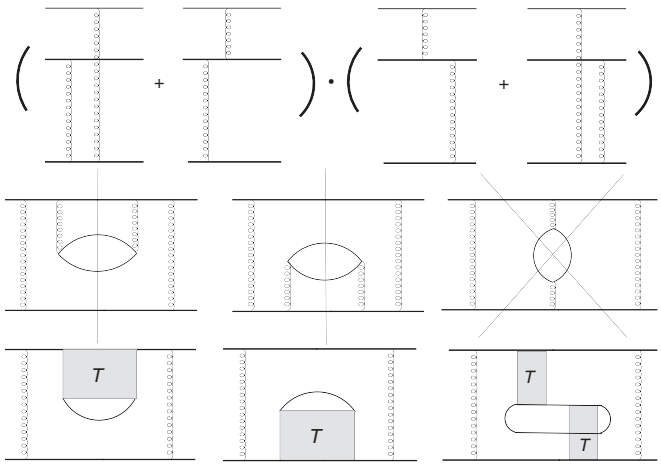

FIG. 13. The first row depicts $\mathcal{M}\cdot\mathcal{M}^\dagger$ including interference effects that can be obtained by cutting the diagrams as shown in the second row. The third row is the T-matrix generalization of the diagrams in the second row.

$TGGT$, in the HQ t-channel interaction form a BSE (i.e., energy-transfer dependent) kernel,

$$K(\tilde{p}-\tilde{p}')=\int d\tilde{k}\,T_{Qq}(\tilde{k},\tilde{k}+\tilde{p}-\tilde{p}')G_q(\tilde{k}+\tilde{p}-\tilde{p}')\times T_{Qq}(\tilde{k}+\tilde{p}-\tilde{p}',\tilde{k})G_q(\tilde{k}),\tag{D1}$$

where $\tilde{p}-\tilde{p}'$ denotes the 4-momentum exchange which introduces complications in the implementation. Taking advantage of the static quarks, we can formulate it in a practically usable form. Transforming the kernel $K(\tilde{p}-\tilde{p}')$ to frequency and coordinate space as $K(\omega_n-\omega_n',r)$, the BSE decouples in coordinate space due to the static limit and forms a matrix equation in frequency space,

$$T(iE_n,i\omega_n,i\omega_n',r)=K(i\omega_n-i\omega_n',r)-\frac{1}{\beta}\sum_{\lambda_n}K(i\omega_n-i\lambda_n,r)\times G(iE_n-i\lambda_n)G(i\lambda_n)T(iE_n,i\lambda_n,i\omega_n',r).\tag{D2}$$

Its solution can be obtained using matrix inversion in analogy to Eq. (15). The continuation to real time is involved due to the complicated analytical structure of the T-matrix, $T(iE_n,i\omega_n,i\omega_n',r)$, and will not be discussed here. Instead, working in imaginary time is enough for our purpose. The BSE solves the equation for an interfering two-body *propagator* with r dependence:

$$G_{Q\bar{Q}}^{(0)}(iE_n,r)=G_{Q\bar{Q}}^0(iE_n)+\left(\frac{-1}{\beta}\right)^2\sum_{\omega_n,\omega_n'}G_Q(i\omega_n)G_{\bar{Q}}(iE_n-i\omega_n)\times T(iE_n,i\omega_n,i\omega_n',r)G_Q(i\omega_n')G_{\bar{Q}}(iE_n-i\omega_n').\tag{D3}$$

The full four-point Green's function is solved by a T-matrix using this propagator with a bare $V(r)$ as kernel:

$$G_{Q\bar{Q}}(iE_n,r)=\frac{1}{\left[G_{Q\bar{Q}}^0(iE_n,r)\right]^{-1}-V(r)}=\frac{1}{iE_n-2\Delta M_Q-V(r)-\Sigma_{Q\bar{Q}}(iE_n,r)}.\tag{D4}$$

Therefore, $\Sigma_{Q\bar{Q}}(z,r)$ in Eq. (49) is defined and calculated by the above setup in terms of $V(r)$, too. With this setup, the evaluation of $F_{Q\bar{Q}}(r,\beta)$ only depends on $V(r)$. Everything else will be generated through the self-consistent many-body field theory framework. With Eq. (C2), the theoretical formalism for the potential is in a closed form, where the only input is the potential $V(r)$, defining a fully constrained functional equation for $V(r)$. This is the example that was referred to after Eq. (44), showing how to start from the bare $V(r)$ to obtain a dispersive $V(z,r)$ or, equivalently, $\Sigma_{Q\bar{Q}}(z,r)$.

The incorporation of loop effects in the t-channel exchange "potential" via a self-consistent evaluation of the self-energy is more rigorous than just forming a closed two-body equation as discussed in this section. The proper procedure should be based on a conserving approximation [19,20] formed by

the Φ derivative. This is not guaranteed for the kernel K, and this is why in the main part of this paper we have only used it to investigate the four-point Green's function, not to implement it to calculate the self-energy. As we have illustrated in Fig. 13, interference effects are inherently three-body processes. Therefore, the self-consistent treatment of interference effects requires a three-body equation, e.g., a Faddeev equation [78]. However, the loop corrections to the in-medium potential are in general different when generating them through a BSE kernel compared to starting from a 3-body Faddeev approach and then contracting the in-medium light-parton line, which is illustrated in Fig. 14. However, one can prove that in the Faddeev-based approach, there is an approximate four-point Green's function that can be cast into a two-body propagator of the form of Eq. (49) or Eq. (D4). The more rigorous treatment of the three-body equation is computational involved and provides an interesting topic for future investigations.

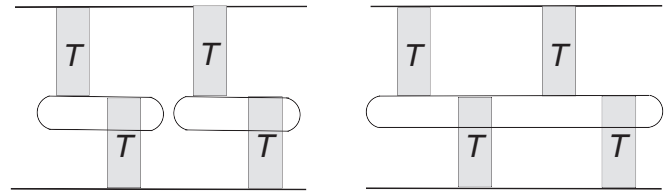

FIG. 14. The left panel shows the diagram corresponding to the BSE implementation of loop effects in the potential, while the right panel is based on a Faddeev equation for the $Q\bar{Q}$+light-parton interaction with the thermal light-parton line being closed off.

[1] P. Braun-Munzinger, V. Koch, T. Schäfer, and J. Stachel, Phys. Rep. **621**, 76 (2016).
[2] D. Teaney, J. Lauret, and E. V. Shuryak, Phys. Rev. Lett. **86**, 4783 (2001).
[3] U. W. Heinz, Landolt-Börnstein **23**, 240 (2010).
[4] C. Gale, S. Jeon, and B. Schenke, Int. J. Mod. Phys. A **28**, 1340011 (2013).
[5] F. Prino and R. Rapp, J. Phys. G **43**, 093002 (2016).
[6] E. Shuryak, Rev. Mod. Phys. **89**, 035001 (2017).
[7] J.-P. Blaizot, E. Iancu, and A. Rebhan, in *Quark Gluon Plasma*, edited by R. C. Hwa and X.-N. Wang (World Scientific, Singapore, 2003), pp. 60–122.
[8] D. H. Rischke, Prog. Part. Nucl. Phys. **52**, 197 (2004).
[9] E. V. Shuryak and I. Zahed, Phys. Rev. D **70**, 054507 (2004).
[10] M. Mannarelli and R. Rapp, Phys. Rev. C **72**, 064905 (2005).
[11] D. Cabrera and R. Rapp, Phys. Rev. D **76**, 114506 (2007).
[12] H. van Hees, M. Mannarelli, V. Greco, and R. Rapp, Phys. Rev. Lett. **100**, 192301 (2008).
[13] F. Riek and R. Rapp, Phys. Rev. C **82**, 035201 (2010).
[14] F. Riek and R. Rapp, New J. Phys. **13**, 045007 (2011).
[15] K. Huggins and R. Rapp, Nucl. Phys. A **896**, 24 (2012).
[16] Y. Burnier, O. Kaczmarek, and A. Rothkopf, Phys. Rev. Lett. **114**, 082001 (2015).
[17] S. Y. F. Liu and R. Rapp, Nucl. Phys. A **941**, 179 (2015).
[18] J. M. Luttinger and J. C. Ward, Phys. Rev. **118**, 1417 (1960).
[19] G. Baym and L. P. Kadanoff, Phys. Rev. **124**, 287 (1961).
[20] G. Baym, Phys. Rev. **127**, 1391 (1962).
[21] S. Y. F. Liu and R. Rapp, J. Phys. Conf. Ser. **779**, 012034 (2017).
[22] S. Godfrey and N. Isgur, Phys. Rev. D **32**, 189 (1985).
[23] S. Capstick and N. Isgur, Phys. Rev. D **34**, 2809 (1986).
[24] W. Lucha, F. F. Schoberl, and D. Gromes, Phys. Rep. **200**, 127 (1991).
[25] S. Y. F. Liu and R. Rapp, arXiv:1612.09138.
[26] E. E. Salpeter and H. A. Bethe, Phys. Rev. **84**, 1232 (1951).
[27] R. Blankenbecler and R. Sugar, Phys. Rev. **142**, 1051 (1966).
[28] R. H. Thompson, Phys. Rev. D **1**, 110 (1970).
[29] R. M. Woloshyn and A. D. Jackson, Nucl. Phys. B **64**, 269 (1973).
[30] F. J. Dyson, Phys. Rev. **85**, 631 (1952).
[31] S. Weinberg, *The Quantum Theory of Fields. Vol. 2: Modern Applications* (Cambridge University Press, Cambridge, 2013).
[32] L. P. Kadanoff and G. A. Baym, *Quantum Statistical Mechanics* (Benjamin, London, 1962).
[33] W.-D. Kraeft, D. Kremp, W. Ebeling, and G. Röpke, *Quantum Statistics of Charged Particle Systems* (Springer, Berlin, 1986).
[34] P.-A. Pantel, D. Davesne, and M. Urban, Phys. Rev. A **90**, 053629 (2014); **94**, 019901 (2016).
[35] J. I. Kapusta and C. Gale, *Finite-temperature Field Theory: Principles and Applications* (Cambridge University Press, Cambridge, 2006).
[36] R. Brockmann and R. Machleidt, Phys. Rev. C **42**, 1965 (1990).
[37] M. Schmidt, G. Röpke, and H. Schulz, Ann. Phys. **202**, 57 (1990).
[38] R. Rapp and J. Wambach, Phys. Rev. C **53**, 3057 (1996).
[39] G. Lacroix, C. Semay, D. Cabrera, and F. Buisseret, Phys. Rev. D **87**, 054025 (2013).
[40] G. Lacroix, C. Semay, and F. Buisseret, Phys. Rev. C **91**, 065204 (2015).
[41] G. E. Brown, C.-H. Lee, M. Rho, and E. Shuryak, Nucl. Phys. A **740**, 171 (2004).
[42] P. Petreczky and K. Petrov, Phys. Rev. D **70**, 054503 (2004).
[43] M. I. Haftel and F. Tabakin, Nucl. Phys. A **158**, 1 (1970).
[44] A. L. Fetter and J. D. Walecka, *Quantum Theory of Many-particle Systems* (Courier Dover Publications, Mineola, NY, 2003).
[45] S. Borsanyi, G. Endrodi, Z. Fodor, A. Jakovac, S. D. Katz, S. Krieg, C. Ratti, and K. K. Szabo, J. High Energy Phys. 11 (2010) 077.
[46] A. Bazavov, T. Bhattacharya, C. DeTar, H.-T. Ding, S. Gottlieb, R. Gupta, P. Hegde, U. M. Heller, F. Karsch, E. Laermann, L. Levkova, S. Mukherjee, P. Petreczky, C. Schmidt, C. Schroeder, R. A. Soltz, W. Soeldner, R. Sugar, M. Wagner, and P. Vranas (HotQCD Collaboration), Phys. Rev. D **90**, 094503 (2014).
[47] O. Kaczmarek and F. Zantow, Phys. Rev. D **71**, 114510 (2005).
[48] A. Mocsy, f. Petreczky, and M. Strickland, Int. J. Mod. Phys. A **28**, 1340012 (2013).
[49] S. Datta, F. Karsch, P. Petreczky, and I. Wetzorke, Phys. Rev. D **69**, 094507 (2004).
[50] A. Jakovac, P. Petreczky, K. Petrov, and A. Velytsky, Phys. Rev. D **75**, 014506 (2007).
[51] G. Aarts, C. Allton, M. B. Oktay, M. Peardon, and J.-I. Skullerud, Phys. Rev. D **76**, 094513 (2007).

[52] G. Aarts, C. Allton, S. Kim, M. P. Lombardo, M. B. Oktay, S. M. Ryan, D. K. Sinclair, and J. I. Skullerud, J. High Energy Phys. 11 (2011) 103.
[53] J. P. Blaizot, E. Iancu, and A. Rebhan, Phys. Rev. D **63**, 065003 (2001).
[54] D. Blaschke, A. Dubinin, and L. Turko, arXiv:1611.09845.
[55] J.-P. Blaizot and G. Ripka, *Quantum Theory of Finite Systems* (MIT Press, Cambridge, MA, 1986).
[56] R. Haussmann, W. Rantner, S. Cerrito, and W. Zwerger, Phys. Rev. A **75**, 023610 (2007).
[57] R. Rapp and J. Wambach, Phys. Lett. B **315**, 220 (1993).
[58] A. Rothkopf, T. Hatsuda, and S. Sasaki, Phys. Rev. Lett. **108**, 162001 (2012).
[59] A. Beraudo, J.-P. Blaizot, and C. Ratti, Nucl. Phys. A **806**, 312 (2008).
[60] M. Laine, O. Philipsen, P. Romatschke, and M. Tassler, J. High Energy Phys. 03 (2007) 054.
[61] Y. Burnier, O. Kaczmarek, and A. Rothkopf, J. High Energy Phys. 12 (2015) 101.
[62] E. Megias, E. Ruiz Arriola, and L. Salcedo, J. High Energy Phys. 01 (2006) 073.
[63] E. Megias, E. R. Arriola, and L. L. Salcedo, Phys. Rev. D **75**, 105019 (2007).
[64] A. Beraudo, J. Blaizot, P. Faccioli, and G. Garberoglio, Nucl. Phys. A **846**, 104 (2010).
[65] M. He, R. J. Fries, and R. Rapp, Phys. Rev. C **86**, 014903 (2012).
[66] X. Zhao and R. Rapp, Phys. Rev. C **82**, 064905 (2010).
[67] Y. Liu, B. Chen, N. Xu, and P. Zhuang, Phys. Lett. B **697**, 32 (2011).
[68] A. Emerick, X. Zhao, and R. Rapp, Eur. Phys. J. A **48**, 72 (2012).
[69] M. Strickland and D. Bazow, Nucl. Phys. A **879**, 25 (2012).
[70] L. Grandchamp and R. Rapp, Phys. Lett. B **523**, 60 (2001).
[71] H. Berrehrah, E. Bratkovskaya, T. Steinert, and W. Cassing, Int. J. Mod. Phys. E **25**, 1642003 (2016).
[72] R. Rapp and X. Du, Nucl. Phys. A **967**, 216 (2017).
[73] P. Petreczky and J. Weber, Nucl. Phys. A **967**, 592 (2017).
[74] S. Y. F. Liu, M. He, and R. Rapp (unpublished).
[75] T. Bhattacharya, M. I. Buchoff, N. H. Christ, H.-T. Ding, R. Gupta, C. Jung, F. Karsch, Z. Lin, R. D. Mawhinney, G. McGlynn, S. Mukherjee, D. Murphy, P. Petreczky, D. Renfrew, C. Schroeder, R. A. Soltz, P. M. Vranas, and H. Yin (HotQCD Collaboration), Phys. Rev. Lett. **113**, 082001 (2014).
[76] E. Shuryak and I. Zahed, Phys. Rev. D **69**, 046005 (2004).
[77] A. Bazavov, Y. Burnier, and P. Petreczky, Nucl. Phys. A **932**, 117 (2014).
[78] L. D. Faddeev, Sov. Phys. JETP **12**, 1014 (1961).